

AD613931

AD No.

DDC FILE COPY

✓  
*Bee*

THE DIMENSIONAL STABILITY OF  
SELECTED ALLOY SYSTEMS

COPY	OF
HARD COPY	\$.
MICROFICHE	\$.

*947*

*Reference Only as DDC Filed Service*

Final Report

June 1, 1963 to August 31, 1964

Prepared under:

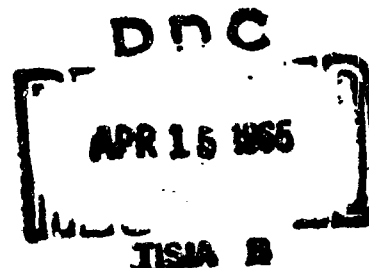
Contract No. N140(131)75098B  
Naval Applied Science Laboratory  
New York Naval Shipyard  
Brooklyn 1, New York

Development, Engineering,  
and Manufacturing  
high and ultra high  
vacuum equipment  
electron beam equipment  
advanced materials  
research

**ALLOYD GENERAL CORPORATION**

MAIN OFFICES: 37 CAMBRIDGE PKY., CAMBRIDGE, MASS. 02142 PHONE 868-6900, AREA CODE 617

PROCESSING COPY  
ARCHIVE COPY



**THE DIMENSIONAL STABILITY OF  
SELECTED ALLOY SYSTEMS**

**By:**

**P.F. Wehrauch  
M.J. Hordon**

**Final Report**

**June 1, 1963 to August 31, 1964**

**Prepared under:**

**Contract No. N140(131)750982  
Naval Applied Science Laboratory  
New York Naval Shipyard  
Brooklyn 1, New York**

**Submitted by:**

**Alloyd General Corporation  
57 Cambridge Parkway  
Cambridge 42, Massachusetts**

## TABLE OF CONTENTS

	<u>Page</u>
1. INTRODUCTION.....	1
2. MATERIALS AND PREPARATION.....	2
3. EXPERIMENTAL PROCEDURE.....	5
4. RESULTS AND DISCUSSION.....	21
5. DISTORTION MEASUREMENT FACILITY.....	77
6. FUTURE WORK.....	83
7. REFERENCES.....	84

## LIST OF TABLES

I. Chemical Composition of Specimen Materials	3
II. Heat Treating and Machining Schedules	4
III. Applied Creep Stresses	17
IV. Elastic Limits and Elastic Moduli of Three Alloys at 75, 150 and 200°F	27
V. Creep Constants for Equation 14	66
VI. Creep Constants for Equation 20	70

## LIST OF FIGURES

	<u>Page</u>
Figure 1 - Schematic view of capacitance gauge and specimen.....	6
Figure 2 - Capacitance gauge test specimen.....	7
Figure 3 - Constant temperature chamber for elastic limit measurements.....	11
Figure 4 - Constant temperature and constant atmosphere chamber for creep measurements.	14
Figure 5 - Storage specimen for dimensional stability testing.....	18
Figure 6 - Stress-total strain and stress plastic strain curves of free cut Invar "36" at 75, 150 and 200°F.....	22
Figure 7 - Stress-total strain and stress plastic strain curves of 356-T6 aluminum at 75, 150 and 200°F.....	23
Figure 8 - Stress-total strain and stress-plastic strain curves of 316 stainless steel at 75, 150 and 200°F.....	24
Figure 9 - Stress-total strain and stress-plastic strain curves of 6061 aluminum at 75, 150 and 200°F.....	25
Figure 10 - Stress-total strain and stress-plastic strain curves of AZ92A magnesium at 75, 150 and 200°F.....	26
Figure 11 - Square root of plastic strain vs. stress for five alloys tested at 75°F.....	28
Figure 12 - Total creep curves of Invar "36" at 85°F..	30

### List of Figures - Continued

	<u>Page</u>
Figure 13 - Total creep curves of Invar "36" at 150°F.	31
Figure 14 - Total creep curves of Invar "36" at 200°F.	32
Figure 15 - Total creep curves of 356-T6 aluminum at 85°F.....	33
Figure 16 - Total creep curves of 356-T6 aluminum at 150°F.....	34
Figure 17 - Total creep curves of 356-T6 aluminum at 200°F.....	35
Figure 18 - Total creep curves of 310 stainless steel at 85°F.....	36
Figure 19 - Total creep curves of 310 stainless steel at 150°F.....	37
Figure 20 - Total creep curves of 310 stainless steel at 200°F.....	38
Figure 21 - Total creep curves of 6061-T6 aluminum at 85°F.....	39
Figure 22 - Total creep curves of 6061-T6 aluminum at 150°F.....	40
Figure 23 - Total creep curves of 6061-T6 aluminum at 200°F.....	41
Figure 24 - Total creep curves of AZ92A magnesium at 85°F.....	42
Figure 25 - Total creep curves of AZ92A magnesium at 150°F.....	43
Figure 26 - Total Creep curves of AZ92A magnesium at 200°F.....	44

# List of Figures - Continued

	<u>Page</u>
Figure 27 - Total creep curves of free cut Invar at 75°F .....	51
Figure 28 - Creep curves of free cut Invar at 150°F ..	52
Figure 29 - Creep curves of free cut Invar at 200°F ..	53
Figure 30 - Creep curves of 356-T6 aluminum at 75°F ..	54
Figure 31 - Creep curves of 356-T6 aluminum at 150°F .	55
Figure 32 - Creep curves of 356-T6 aluminum at 200°F .	56
Figure 33 - Creep curves of 310 stainless steel at 75°F .....	57
Figure 34 - Creep curves of 310 stainless steel at 150°F .....	58
Figure 35 - Creep curves of 310 stainless steel at 200°F .....	59
Figure 36 - Creep curves of 6061 aluminum at 75°F ....	60
Figure 37 - Creep curves of 6061 aluminum at 150°F ...	61
Figure 38 - Creep curves of 6061 aluminum at 200°F ...	62
Figure 39 - Creep curves of AZ92A - T6 magnesium at 75°F .....	63
Figure 40 - Creep curves of AZ92A magnesium at 150°F .	64
Figure 41 - Creep curves of AZ92A magnesium at 200°F .	65
Figure 42 - Dimensional change of free cut Invar 36 stored at 75, 150 and 200°F .....	71
Figure 43 - Dimensional changes of 356-T6 Aluminum stored at 75, 150 and 200°F .....	72

## List of Figures - Continued

	<u>Page</u>
Figure 44 - Dimensional Changes of 310 stainless steel stored at 75, 150 and 200°F.....	73
Figure 45 - Dimensional changes of 6061 Aluminum stored at 75, 150 and 200°F.....	74
Figure 46 - Dimensional change of A292A magnesium stored at 75, 150 and 200°F.....	75
Figure 47 - Distortion specimen.....	78
Figure 48 - Schematic view of distortion measuring facility.....	80



### ABSTRACT

Elastic limits, elastic moduli, stress-total strain and stress-plastic strain curves were determined for free cutting Invar 36, 356-T6 aluminum, 310 stainless steel, 6061 aluminum and AZ92A magnesium at 75, 150 and 200°F. The creep behavior of these alloys was studied at the same temperatures of interest at stresses above, below and at the elastic limit.

In all cases it was found that the precision elastic limit did not define the minimum stress to cause creep, in fact creep took place at stresses below the elastic limit at a much reduced rate. The data was analyzed in the light of current creep theory and micro-yield theory. A dislocation model was used to derive analytic expressions for creep near the  $10^{-6}$  elastic limit stress. Below the elastic limit creep was found to follow an exponential time dependence, while above the elastic limit a  $t^n$  time dependence was followed with values of  $n$  from  $1/3$  to  $1/2$ .

The dimensional changes taking place in these alloys under storage conditions at the three temperatures of interest is also presented.

A facility for measuring distortion as a function of heat treating and machining operations was designed and constructed and is described.

## **I. INTRODUCTION**

The present report summarizes the work undertaken by Alloyd General Corporation during the period June 1, 1963 to August 31, 1964 under the sponsorship of the Naval Applied Science Laboratory, New York Naval Shipyard to investigate the dimensional stability of several alloy systems.

In the course of this program dimensional stability evaluations were made of five alloys, free cut Invar 36, 356-T6 aluminum, 310 stainless steel 6061 aluminum and AZ92 magnesium. An experimental program was developed for determining the dimensional distortion of castings accompanying metal fabricating operations, and the necessary equipment was designed and constructed. Measurements of distortion accompanying heat treating and machining operations were made for castings of type 356-T6 aluminum.

## **2. MATERIALS AND PREPARATION**

### **2.1 Specimen Composition**

The alloys tested were Free Cut Invar "36", 356-T6 aluminum, 310 stainless steel, 6061 aluminum and AZ92A magnesium. The Invar and 6061 aluminum were received in the form of 1 inch diameter cold drawn unannealed rod. The 356 aluminum and 310 stainless steel was received as 1 x 1 x 6 inch cast blanks. The magnesium was received in the form of 25 pound cast ingots. The chemical compositions of these alloys are given in Table I.

### **2.2 Heat Treating and Machining Schedule**

The as-received materials were given heat treatments recommended for maximum dimensional stability.<sup>(1)</sup> The heat treating and machining schedules as well as the final hardness of each alloy are presented in Table II.

**TABLE I****Chemical Composition of Specimen Materials**

<b>Element</b>	<b>Invar 36</b>	<b>310 Stainless</b>	<b>Al 356-T6</b>	<b>Al 6061</b>	<b>Mg AZ92A</b>
<b>C</b>	0.12	0.20	-	-	-
<b>Mn</b>	1.00	1.50	-	-	.24
<b>Si</b>	0.35	2.00	7.0	0.6	<.20
<b>Cr</b>	-	23.0	-	0.25	-
<b>Ni+Co</b>	36.0	-	-	-	<.010
<b>Ni</b>	-	19.0	-	-	-
<b>Fe</b>	bal.	bal.	-	-	-
<b>Al</b>	-	-	bal.	bal.	9.0
<b>Mg</b>	-	-	-	1.0	bal.
<b>Cu</b>	-	-	-	0.25	<.04
<b>Zn</b>	-	-	-	-	2.0
<b>Be</b>	-	-	-	-	<.0003

TABLE II

Heat Treating and Machining Schedules

Material

Invar "36"	1. Heat treat 1525°F in hydrogen - 1/2 hour, water quench.
hardness	2. Rough machine to over size dimensions.
Rockwell "B", 85	3. Heat treat 1200°F in hydrogen - air cool.
	4. Final machine
	5. Stabilize 200°F - 48 hours, air cool.
310 stainless steel	1. Quench Anneal 1950°F in hydrogen - 1/2 hour, water quench.
hardness	2. Rough machine to oversize dimensions.
Rockwell "B", 83	3. Stress relieve 750°F in air - 1 hour, air cool.
	4. Final machine
	5. Stabilize 200°F - 20 hours, air cool.
356-T6 aluminum	1. Solution anneal - 1000°F in air - 2 hrs.
hardness	2. Quench in boiling water
Rockwell "F", 77	3. Rough machine to oversize dimensions.
	4. Temper 310°F - 4 hours, air cool
	5. Final machine
6061 aluminum	1. Solution anneal - 970°F in air - 2 hrs.
hardness	2. Water quench
Rockwell "B", 55	3. Rough machine to oversize dimensions
	4. Age harden - 350°F, 6 hrs., air cool
	5. Final machine
AZ92A Magnesium	1. Solution anneal - 750°F in SO <sub>2</sub> atmosphere - 20 hrs.
hardness	2. Air blast cool
Rockwell "F", 86	3. Rough machine to oversize dimensions
	4. Age harden - 500°F, 4 hrs., air cool
	5. Final machine

### **3. EXPERIMENTAL PROCEDURE**

#### **3.1 Capacitance Strain Gauge Determinations**

All creep behavior as well as the elastic limit and stress-strain determinations of the alloys were made with a capacitance strain gauge. This gauge (Figure 1) consists of a two piece precision machined invar housing which is mounted on the shoulders of the specimen (Figure 2). A quartz disc plated with platinum on one face is mounted in the upper section and acts as the positive electrode of a parallel plate capacitor. The face of the lower housing is highly polished and acts as the ground electrode of the capacitor. The height of the housing can be varied with the adjustment screws and the gauge sensitivity can be varied within broad limits by changing the capacitor spacing. With this device, changes in specimen length result in a change of capacitor spacing which, in turn, is translated into a change in capacitance.

#### **3.2 Elastic Limit and Stress-Strain Determinations**

The elastic limit of a material is defined as the lowest stress required to produce a measurable amount of plastic strain. The method used in these determinations was the load-unload technique of Muir and Averbach.<sup>(2)</sup>

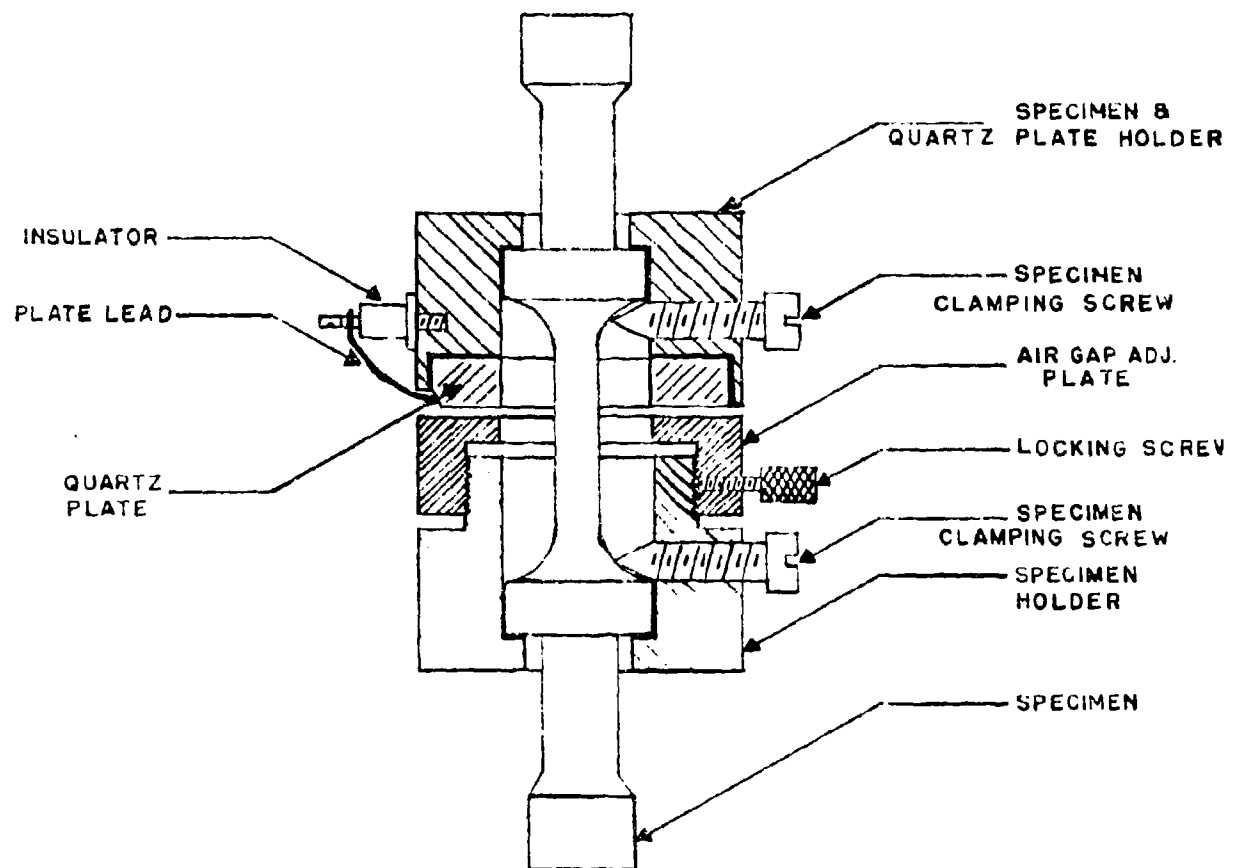


FIGURE 1 . SCHEMATIC VIEW OF CAPACITANCE GAUGE  
AND SPECIMEN



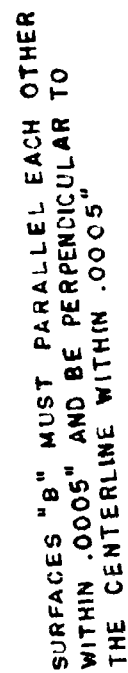


FIGURE 2 CAPACITANCE GAUGE TEST SPECIMEN

Tests were conducted in an Instron gear-driven testing machine of 10,000 pounds capacity. The 500 and 1000 pound scales were used and loads were read to the nearest 5 and 10 pounds, respectively. The test specimen, shown in Figure 2, was gripped against its 45° shoulders by matched split nuts which were threaded into grips. The grips were connected to the frame and cross-head of the machine by mild steel rods hangers through spherical rod-end bearings. Loads were applied in increments of 400 psi in the region of the anticipated elastic limit. The loading rate was approximately 20,000 psi per minute and the specimen was immediately unloaded on reaching the desired stress. Repeatable "zero" stress conditions were achieved by allowing the specimen to hang freely under the weight of the lower grip and hanger for unloaded strain readings. All the components of the gripping system were precision machined to maintain axiality of loading.

Upon reaching the elastic limit the load-unload sequence was continued until the macroscopic yield point was reached. The change in capacitance was read at the maximum load and upon unloading. In this way the stress-total strain and stress-plastic strain curves were generated.

The change in gauge capacitance was measured with a Robertshaw and Fulton Proximity Meter. Meter calibration was carried out for each specimen by loading the specimen to stresses well below the elastic limit and noting the meter deflection. There are six meter scale factors which allow strain measurements to be made in a range from  $1 \times 10^{-7}$  to  $800 \times 10^{-6}$  inches/inch. The calibration was found to be linear over this range as evidenced by comparison with electrical resistance strain-gauge measurements. The maximum strain sensitivity achieved with the capacitance gauge was  $1 \times 10^{-7}$  inches/inch, however, difficulties in temperature control caused thermal expansion and contraction during the load-unload cycle which, in some cases, dwarfed length changes due to plastic strain. As a result the strain sensitivity used was  $5 \times 10^{-7}$  inches/inch.

Testing was carried out at three temperatures; 75, 150 and 200°F. The room temperature tests (75°F) were carried out in air without temperature control. Due to the large thermal mass of the specimen-capacitance gauge configuration, temperature fluctuations took place very slowly so that expansion or contraction during any load-

unload cycle was less than  $5 \times 10^{-7}$  inches/inch. At the higher temperature (150 and 200°F) testing was carried out in a temperature controlled air chamber. The apparatus (see Figure 3) consisted of an annular container. The inner cylinder of the container was a nichrome wound resistance furnace and served as a constant temperature enclosure for the specimen and grips. The temperature was controlled to within  $\pm 1^\circ\text{F}$  by a thermocouple controller. The temperature was read independently with an iron-constantan thermocouple mounted on the specimen.

### 3.3 Elastic Modulus Measurements

Since the Proximity Meter does not give absolute values of strain and must be calibrated for each specimen, it is necessary to measure the elastic modulus independently at each temperature. To accomplish this, etched foil electrical resistance strain gauges were bonded to the gauge section of the specimen with EPY-400 epoxy cement. Two gauges mounted on opposite sides of the specimen and wired in series were used to balance any effect due to nonaxiality of loading and to produce a reading of average strain. The gauges were moisture proofed with a coat of Stycast 2651 high temperature epoxy.

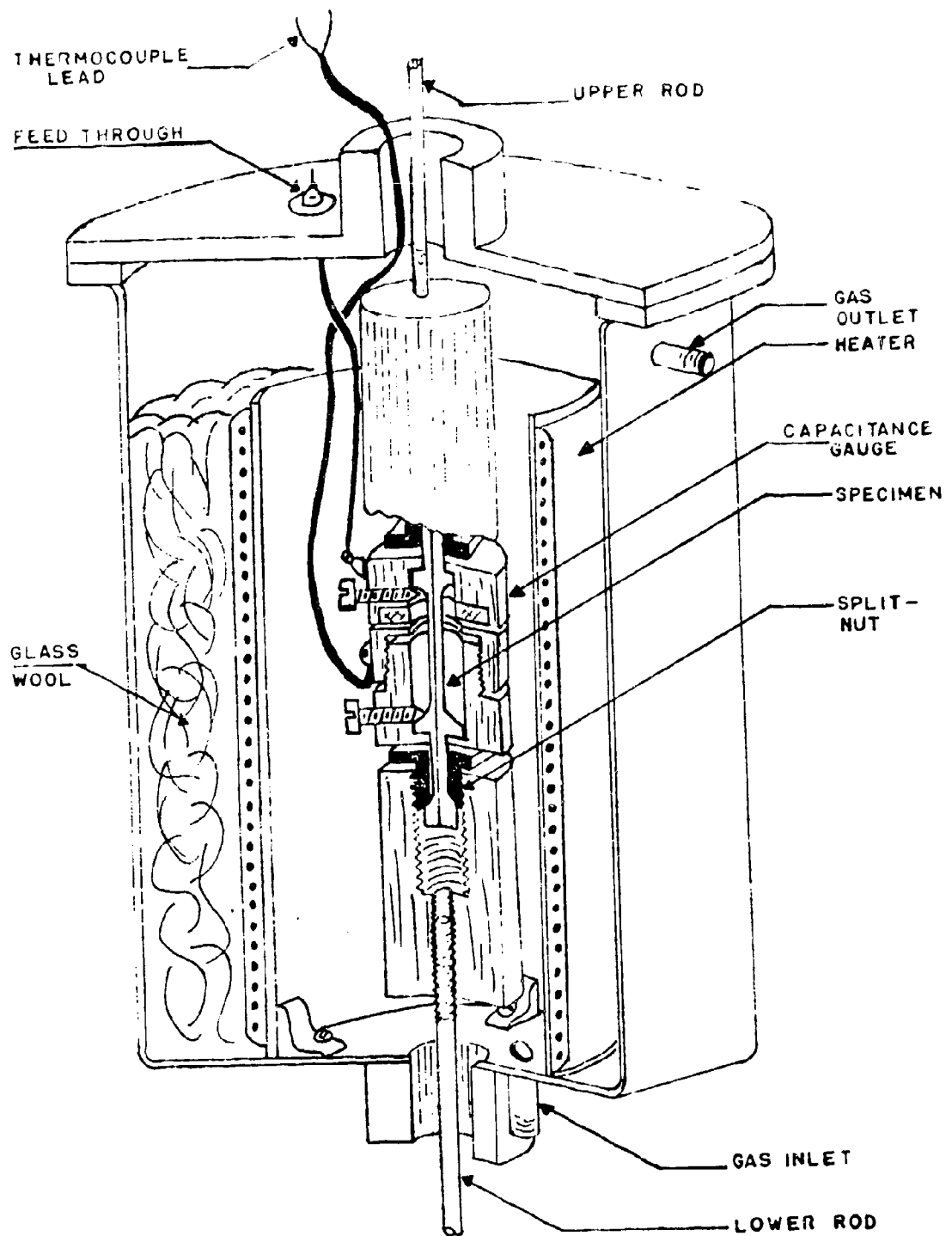


FIGURE 3. CONSTANT TEMPERATURE CHAMBER FOR ELASTIC LIMIT MEASUREMENTS

For tests at ambient temperature a similarly prepared unstressed specimen was mounted near the test specimen to act as a temperature compensator. At 150°F and 200°F the unstressed specimen was mounted in an air furnace and independently maintained at temperature. Both the test specimen and compensator specimen temperatures were monitored with iron-constantan thermocouples. For room temperature tests no temperature control was necessary since the ambient did not vary more than  $\pm 0.2^\circ\text{F}$  during the short testing times. The stress values were read on the Instron Chart to an accuracy of  $\pm 100$  psi and the strain values to  $\pm 2 \times 10^{-6}$  inches/inch with a Baldwin type W strain indicator.

A stress was applied below the elastic limit and the strain was measured. Five independent measurements were made for each specimen at each temperature and the modulus was calculated. The five values were then averaged.

### 3.4 Creep Tests

Creep tests were conducted in a bank of six dead-load creep machines using an interrupted loading

technique. The test specimen was enclosed in a constant temperature and constant atmosphere chamber which was mounted on supports connected to the creep frame (see Figure 4). The temperature was maintained by a tubular nichrome wound resistance furnace and controlled by a thermistor element to  $\pm 0.1^\circ\text{F}$ . Nitrogen was continuously fed into the chamber after passing through a drying and heating column.

A creep stress was applied for a period of time and then removed; the stress was measured with a strain gage load cell and the residual strain was measured by the capacitance strain gage. The specimen was then reloaded for a longer period of time. The procedure was continued for increasing periods of time until a total of 500 hours of creep was accumulated.

The strain was measured using the capacitance gauge and the specimen of Figure 1.

The changes in gage capacity were measured with an Electro-Scientific Industries 707A capacitance bridge of variable sensitivity. The meter was calibrated by loading the specimen with known weights and from the stress-strain curve, equating the strain to the meter deflection.

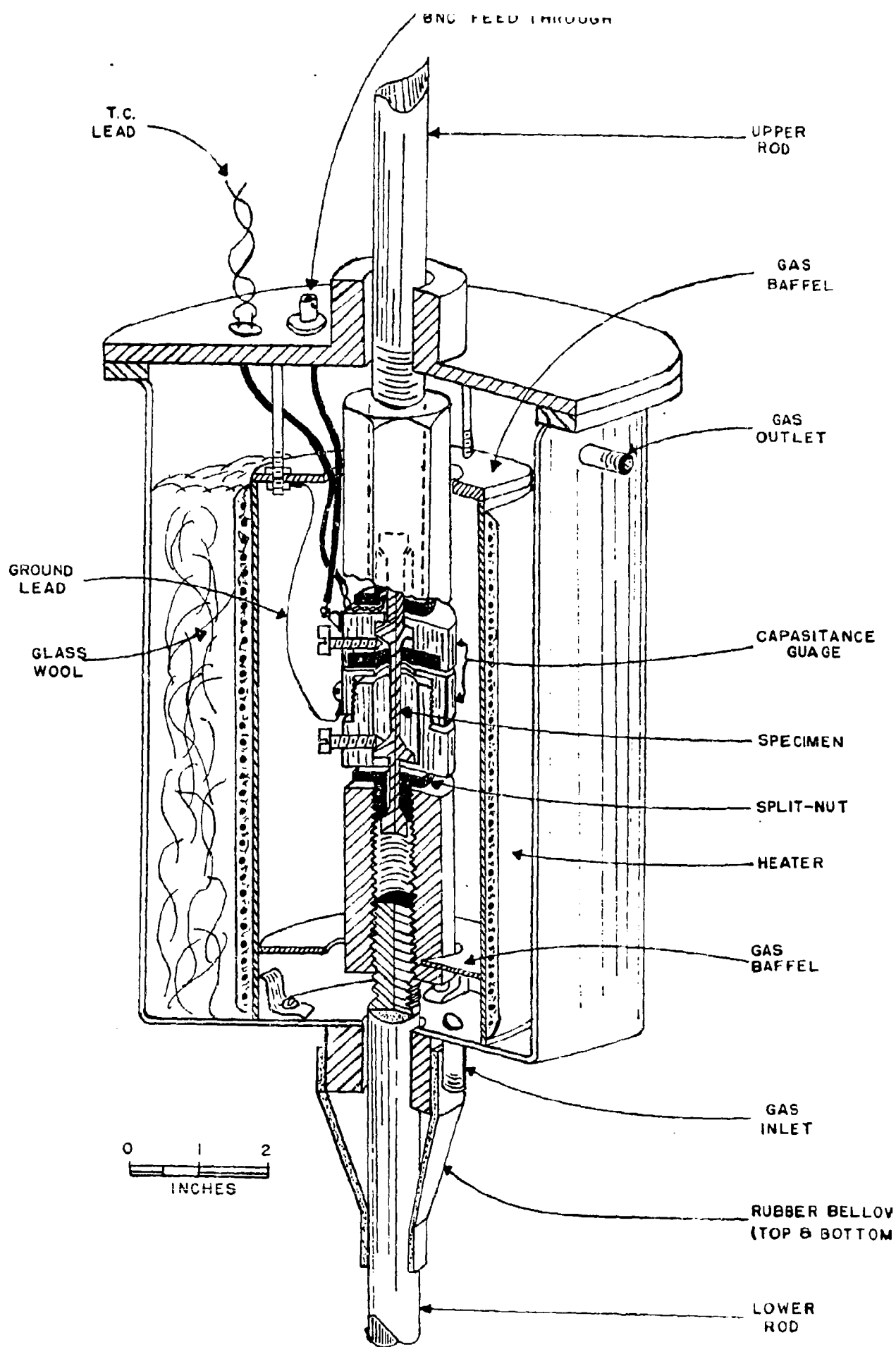


Figure - Constant Temperature and Constant Atmosphere Chamber for Creep Measurements.



Maximum strain resolution of  $2 \times 10^{-7}$  inches per inch is possible with this instrument.

The specimen was gripped against its shoulders by matched split nuts which were threaded into grips. The grips were connected by threaded rods to the upper and lower yokes. The lower yoke, which also served as a load cell for measuring stress, was connected by a spherical thrust bearing to the frame of the machine. The upper yoke was pinned to the lever arm. The lever arm was pivoted on a pin in a support block and could be arranged to give a mechanical advantage of ten or twenty to one. Stress was applied to the creep specimen by means of cast iron weights stacked on a hanger attached to the lever arm. The load was removed by means of a hydraulic jack. For zero readings, the lever arm was held in the unloaded position by a support arm and pin.

The creep stress was measured by means of a load cell in the lower yoke of the creep machine. The cell consisted of a 0.350 inch diameter section of the yoke machined into a 2 inch tensile bar. The tensile bar was instrumented with two etched foil strain gages located on opposite sides of the gage section perpendicular to the

lever arm and wired in series. The strain gages were moisture-proofed with a coating of Stycast 2651 epoxy potting compound. A similar dummy bar was hung next to the load cell as a temperature compensator. A Baldwin type M strain indicator was used for strain readings which were converted to stress by the stress-strain curve of the mild steel rod.

Table III lists the creep stresses and temperatures investigated for each material during this program.

### 3.5 Dimensional Changes with Zero Applied Loads

In order to study the dimensional changes under storage conditions, specimens of the four alloys were machined to the dimensions of Figure 5 following the same heat treating and machining schedule previously outlined. After the final heat treatment the specimens were given a hand polish with 3/0 grit emery paper followed by a careful polish with a fine micropolishing paper.

The specimens were then placed in air furnaces maintained at 75, 150 and 200°F and their lengths periodically measured. The furnace temperature was maintained at  $\pm 0.5^\circ\text{F}$  of the designated temperatures.

**TABLE III**  
**Applied Creep Stresses**

<b><u>Material</u></b>	<b><u>85°F</u></b>	<b><u>150°F</u></b>	<b><u>200°F</u></b>
<b>Free Cut</b>	50,000	48,000	35,000
<b>Invar 36</b>	35,000	33,500	25,000
	22,000	22,000	15,000
<b>356-T6</b>	13,500	12,500	12,000
<b>Aluminum</b>	9,000	8,400	8,200
	6,300	6,100	5,800
<b>310 Stainless</b>	37,500	36,000	34,500
<b>Steel</b>	25,000	24,000	23,000
	16,700	16,000	14,500
<b>6061 Aluminum</b>	25,000	24,000	23,500
	17,500	15,500	15,000
	10,500	9,500	9,000
<b>AZ92A</b>	8,380	8,000	7,400
<b>Magnesium</b>	5,280	5,000	4,780
	3,700	3,530	3,340

Material:

Invar

Aluminum

304 Stainless Steel

304C Stainless Steel

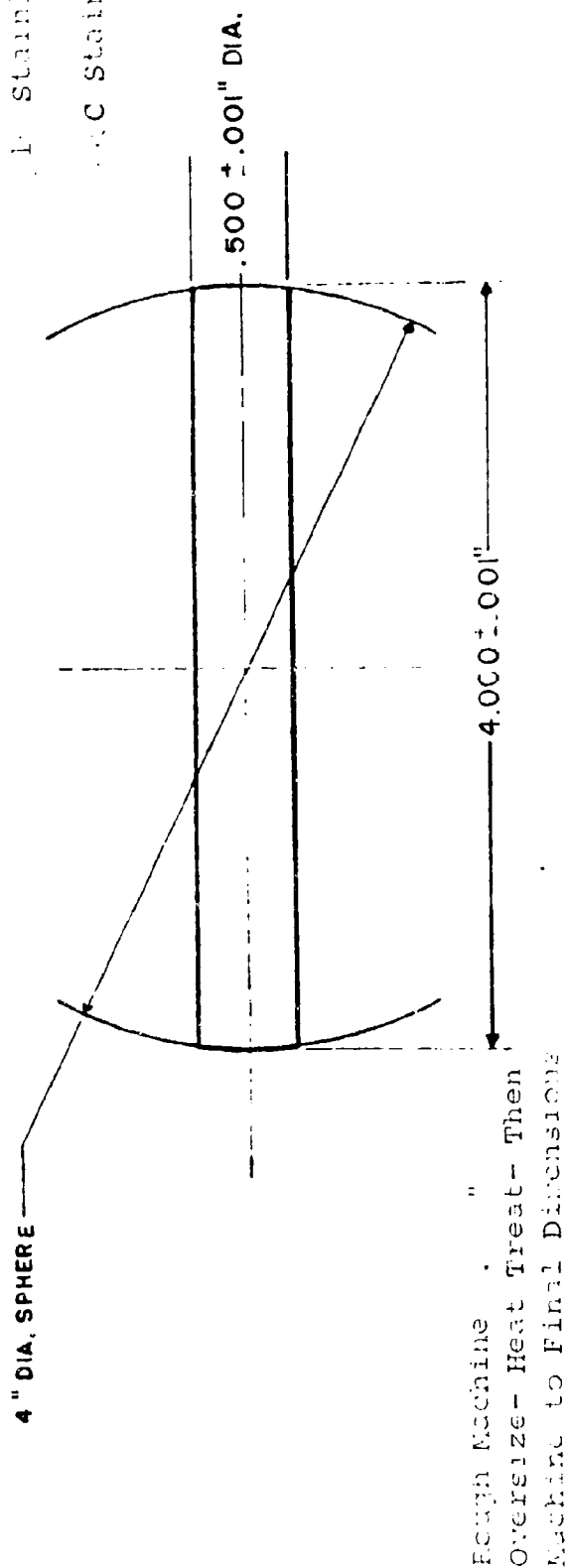


Figure 1 - Storage Specimen for Dimensional Stability Testing.

Dimensional changes were determined from precision measurements of the overall length of the specimen after each storage period. All measurements were made using a Sheffield mechanical optical comparator with an accuracy of  $\pm 5$  microinches/inch. The comparator indicated the difference in length between the test specimen and a gage block of known length.

The nominal finished length of the storage specimens was 4 inches but the length varied from specimen to specimen. Since the scale range of the comparator is 0.001 inches, a single gauge block (4.050 inches in length) was used. When required, a small standard block could be selected from a series of standards and placed under the specimen so that the overall height of the specimen plus block was within 0.001 inches of 4.050 inches.

The storage specimen, upon removal from the furnace, was placed on a large copper block for a period in excess of 30 minutes. Because of its large thermal mass, the copper block served as a constant temperature plate. A reading of the specimen was taken on the comparator and then returned to the copper plate.

The gage block was then read. This procedure was repeated three times and averaged for both specimen and gage block. The relative length of the specimen was calculated from these values. The resolution of the comparator was  $5 \times 10^{-6}$  inches. For a 4 inch specimen length, this resulted in a sensitivity of  $1.25 \times 10^{-6}$  inches per inch. The specimens and gage blocks were handled with gloved hands at all times to reduce heating and moisture changes and handling was kept to a minimum.

#### 4. RESULTS AND DISCUSSION

##### 4.1 Elastic Limits and Microyield Behavior

The stress-total strain and stress-plastic strain curves for the five alloy systems are presented in Figures 6 - 10. All determinations reported were made with the capacitance strain gauge and the elastic limits are the stresses at which the first  $5 \times 10^{-7}$  strain was detected. The elastic limits and elastic moduli are summarized in Table IV. The elastic limits and the elastic moduli showed a similar temperature dependence, but the elastic limits were somewhat more sensitive to temperature. This has been confirmed in other pure metals<sup>(3)</sup> and alloys<sup>(4)</sup> and has been explained by a thermally activated mechanism of dislocation multiplication and motion.

Brown and Lukens<sup>(5)</sup> and Thomas and Averbach<sup>(6)</sup> have observed and explained a parabolic relationship between stress and plastic strain. The room temperature plastic strain curves of Figures 6-10 are replotted in Figure 11 with the stress plotted against the square root of the plastic strain. A straight line dependence was observed confirming the parabolic work hardening law.

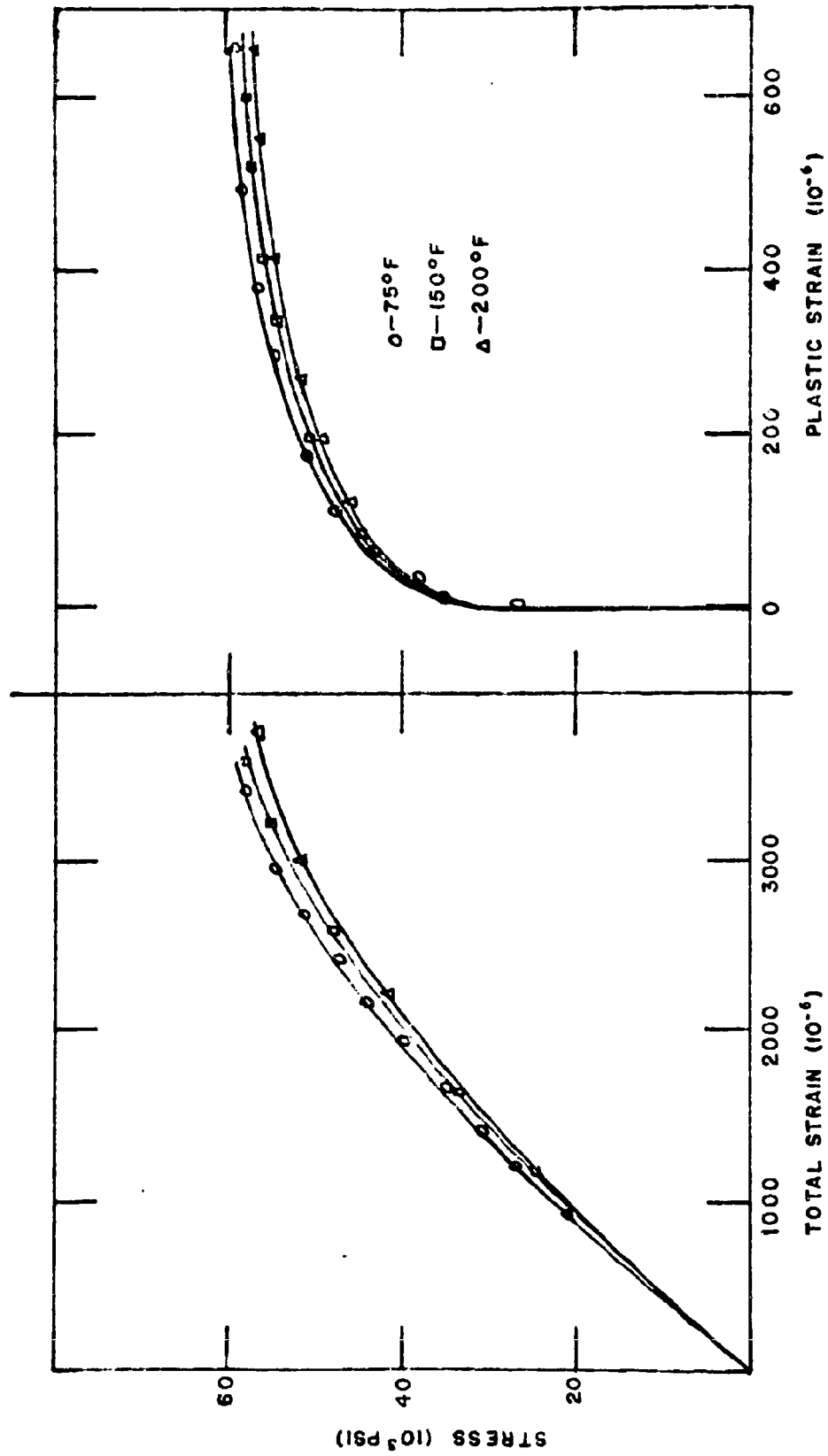


Figure 1 - Stress-total strain and stress-plastic strain curves of free cut Invar "44" at 75, 150 and 200°F.



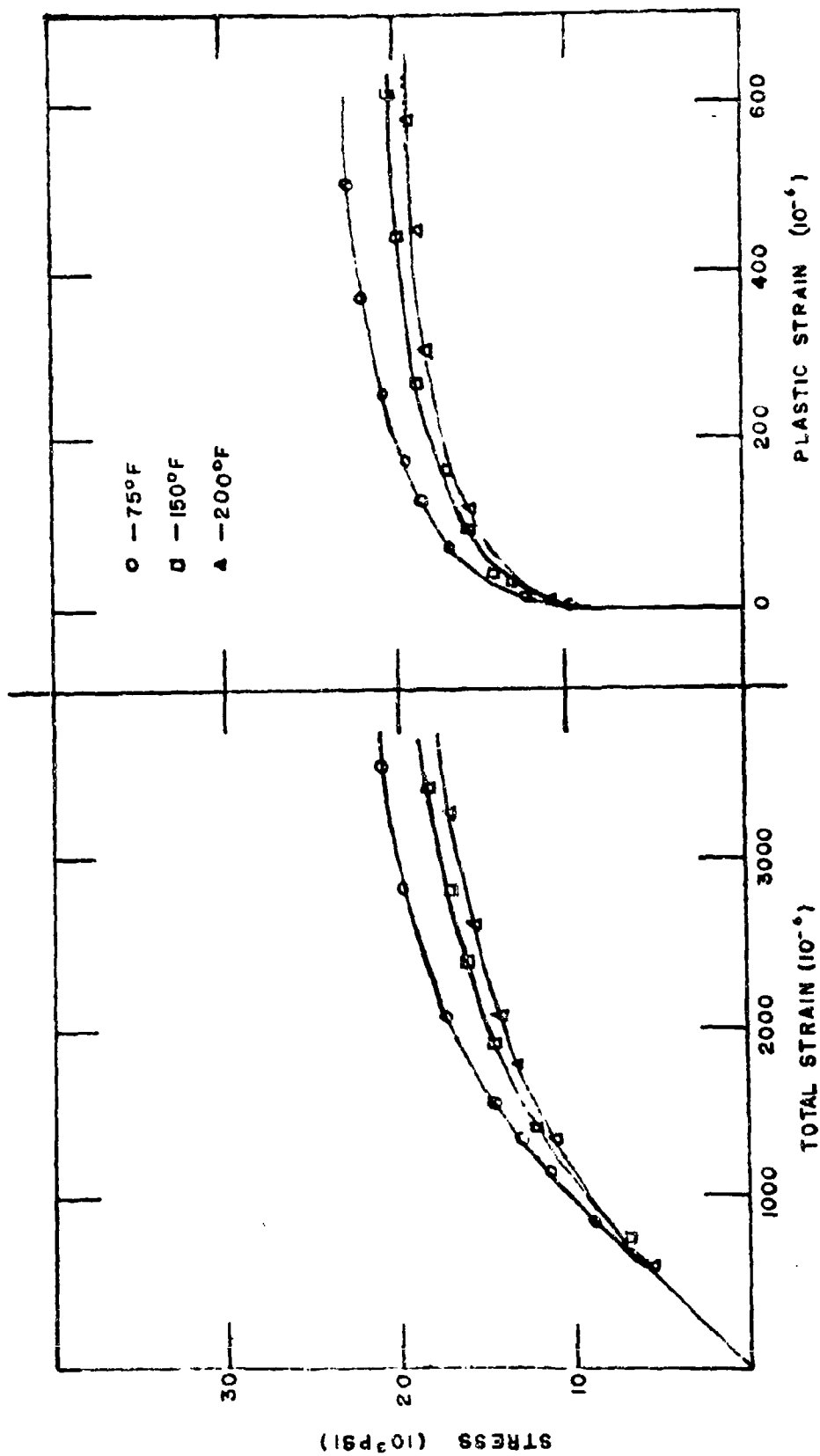


Figure 1 - Stress-total strain and stress-plastic strain curves of 2024-T3 aluminum at -75, -150 and -200°F.

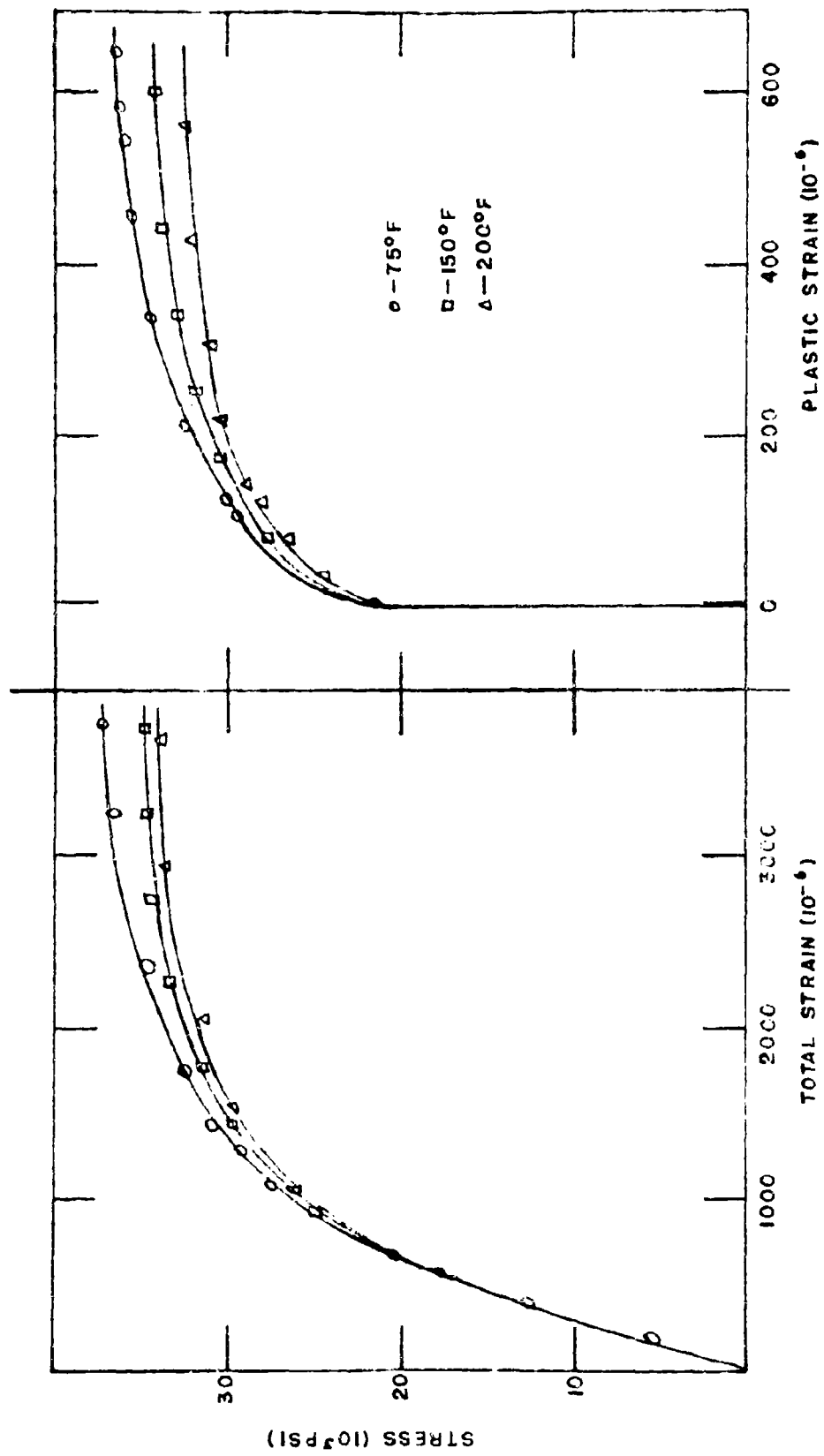


Figure 1 - Stress-total strain and stress-plastic strain curves of 304 stainless steel at 75, 150, and 200°F.

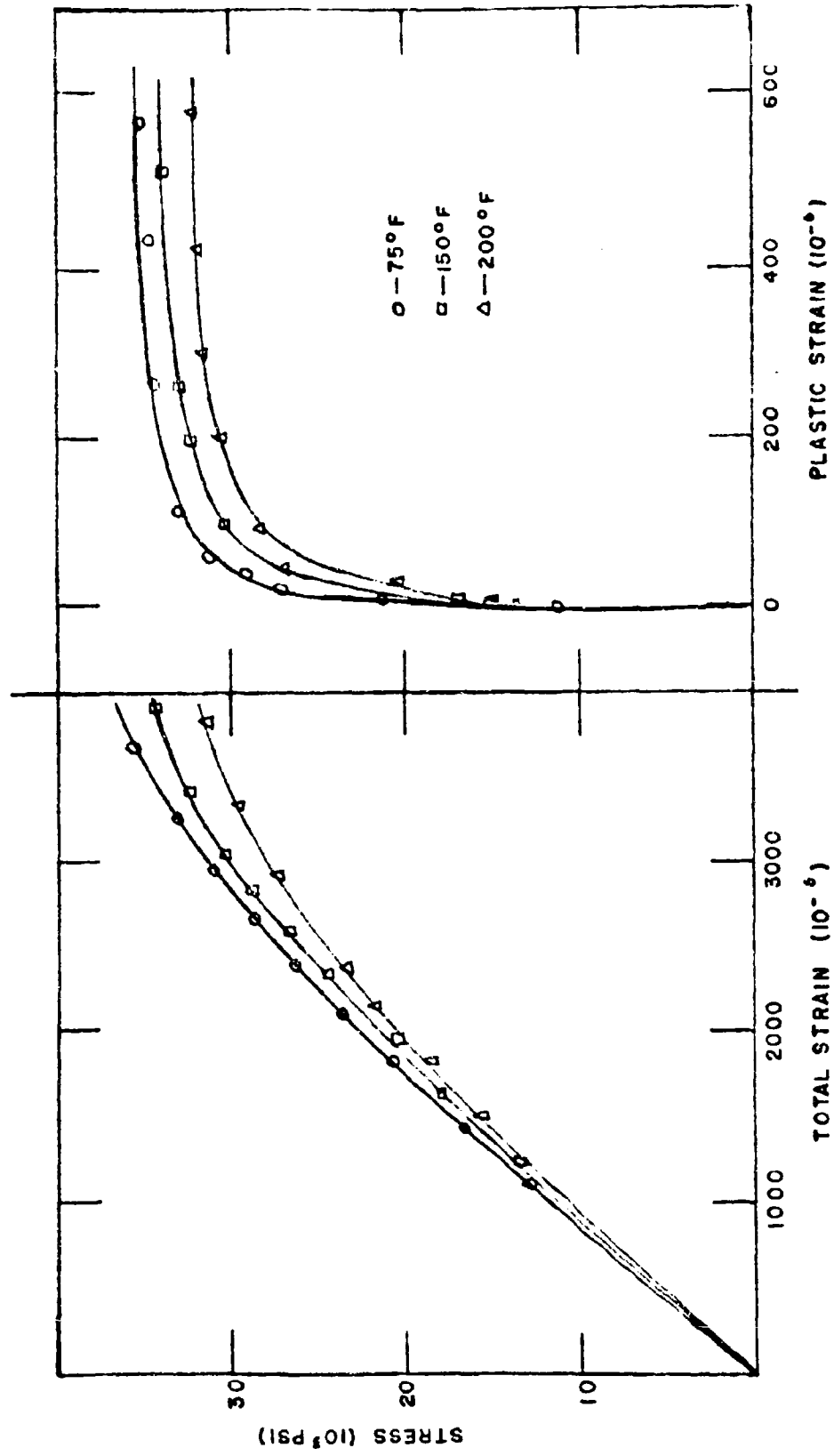


Figure 3 - Stress-total strain and stress-plastic strain curves of 1100 aluminum at 75, 150, and 200°F.

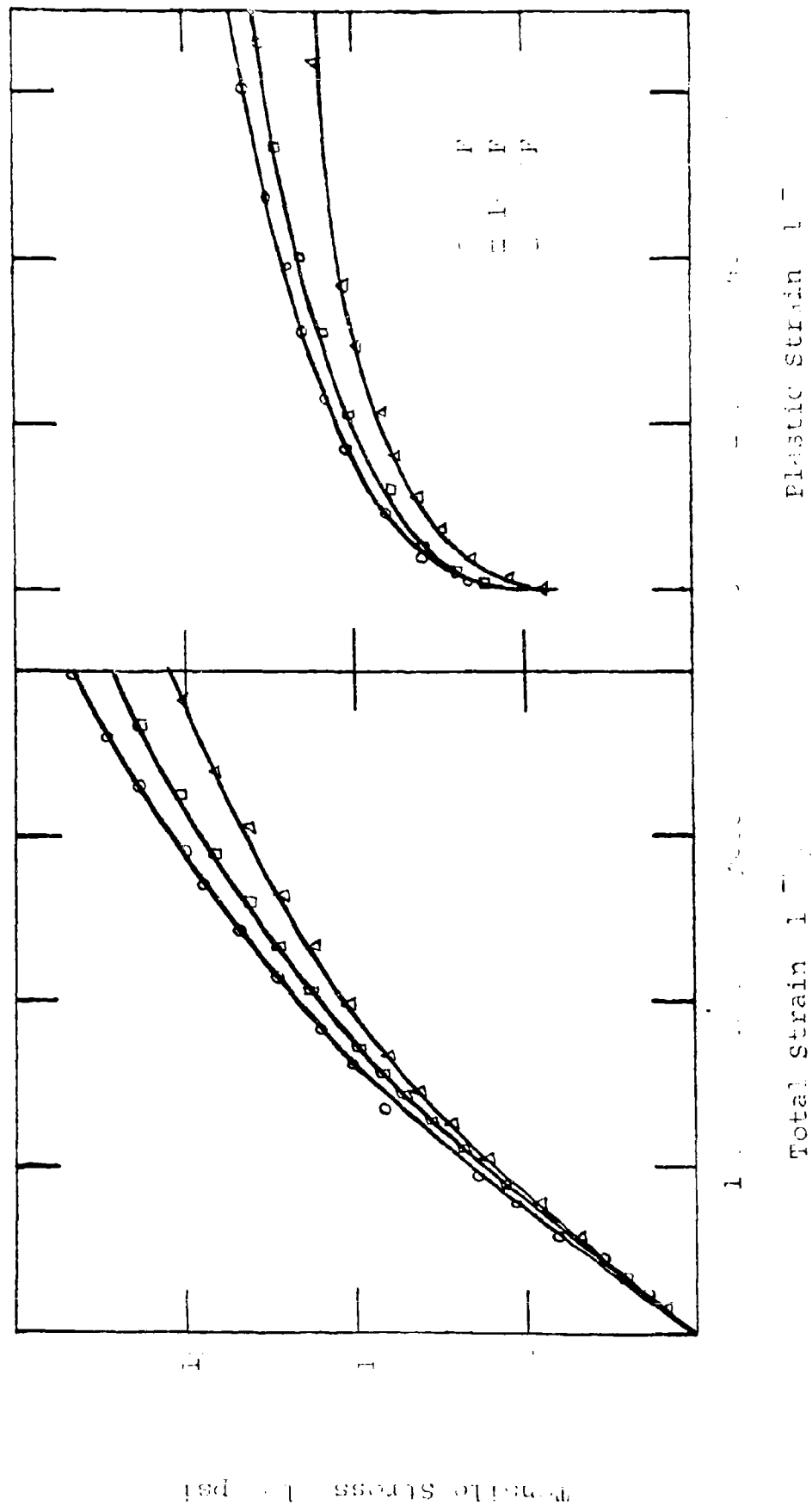


Figure 1. - Stress-total strain and stress-plastic strain curves of 12% magnesium at 0.1% and 1.0% F.

**TABLE IV**

**Elastic Limits and Elastic Moduli of  
Three Alloys at 75, 150 and 200°F**

<u>Material</u>	<u>Test Temperature</u>	<u>Elastic Limit, psi</u>	<u>Elastic Modulus, <math>10^6</math> psi</u>
Invar	75	26,400	23
	150	25,000	22
	200	24,700	21.5
356-T6 Aluminum	75	8,100	11.3
	150	7,350	11.1
	200	7,190	10.9
310 Stainless Steel	75	22,700	29.4
	150	20,400	29.1
	200	20,000	28.7
6061 Aluminum	75	12,400	10.8
	150	11,700	10.5
	200	10,430	10.3
AZ92A Magnesium	75	5,280	6.5
	150	5,040	6.4
	200	4,780	6.1

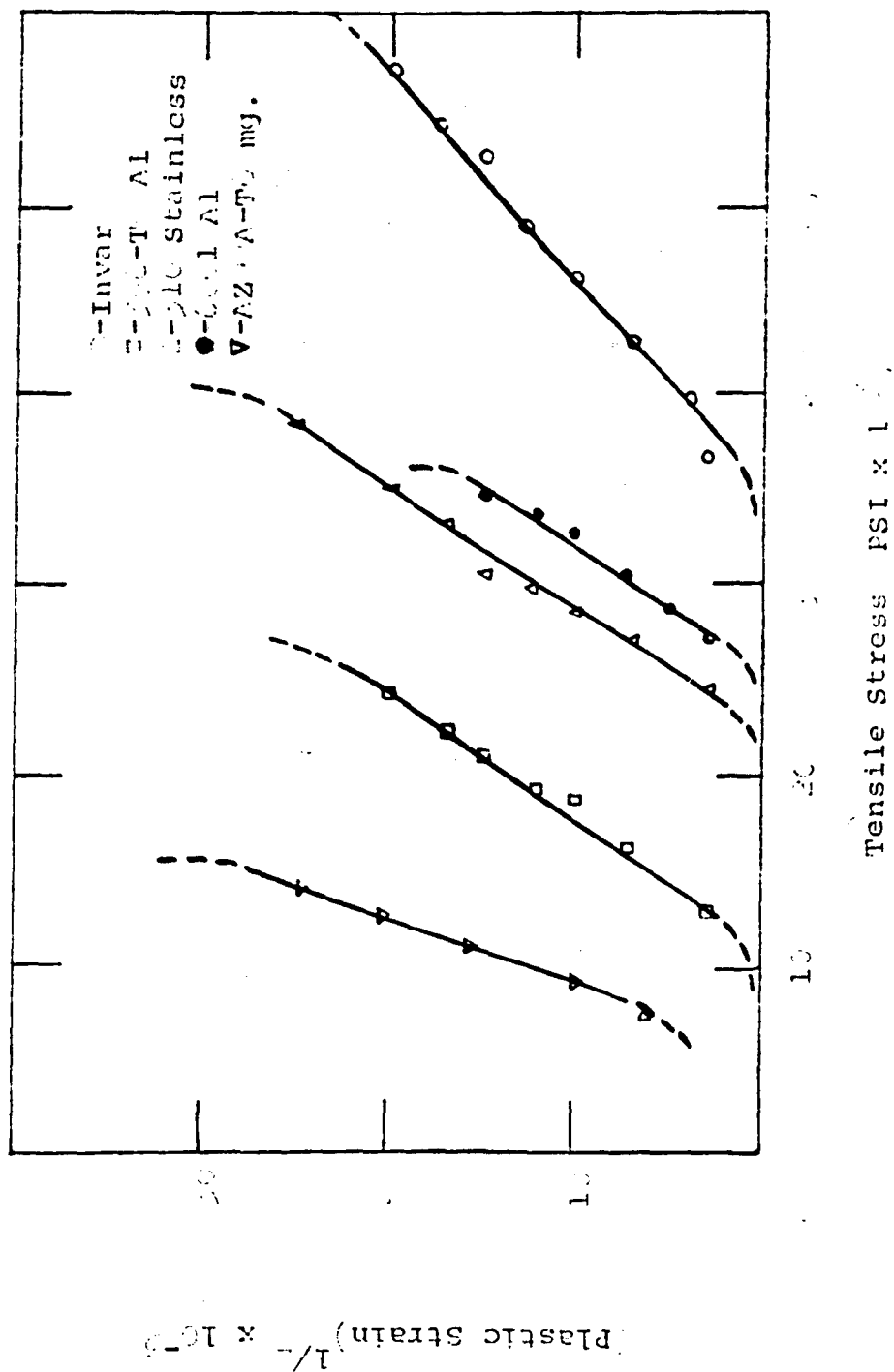


Figure 11 - Square root of plastic strain vs. stress for five alloys tested at 700 F.

#### 4.2 Creep Behavior

The creep behavior under load of free cut Invar 36, 556-T6 aluminum, 310 stainless steel, 6061 aluminum and AZ92P magnesium at 85, 150 and 200°F is presented in Figures 12-26. The creep rate in all cases was seen to start at a high value and decrease continuously until it approached a steady state condition. The early creep rate and creep strain are seen to increase with temperature at comparable stresses.

At creep stresses below the elastic limit the creep rate in all cases decreased continuously approaching zero at the lower temperatures in a short time. Near the elastic limit stress the creep rate decreased continuously approaching a steady state creep rate. At still higher temperatures the creep rate was higher and decreased more slowly.

In order to understand the creep behavior of these alloys it is necessary to develop a dislocation mechanism of creep. Creep at high loads generally consists of three stages, the first of which is characterized by a decreasing creep rate (transient creep). Eventually the

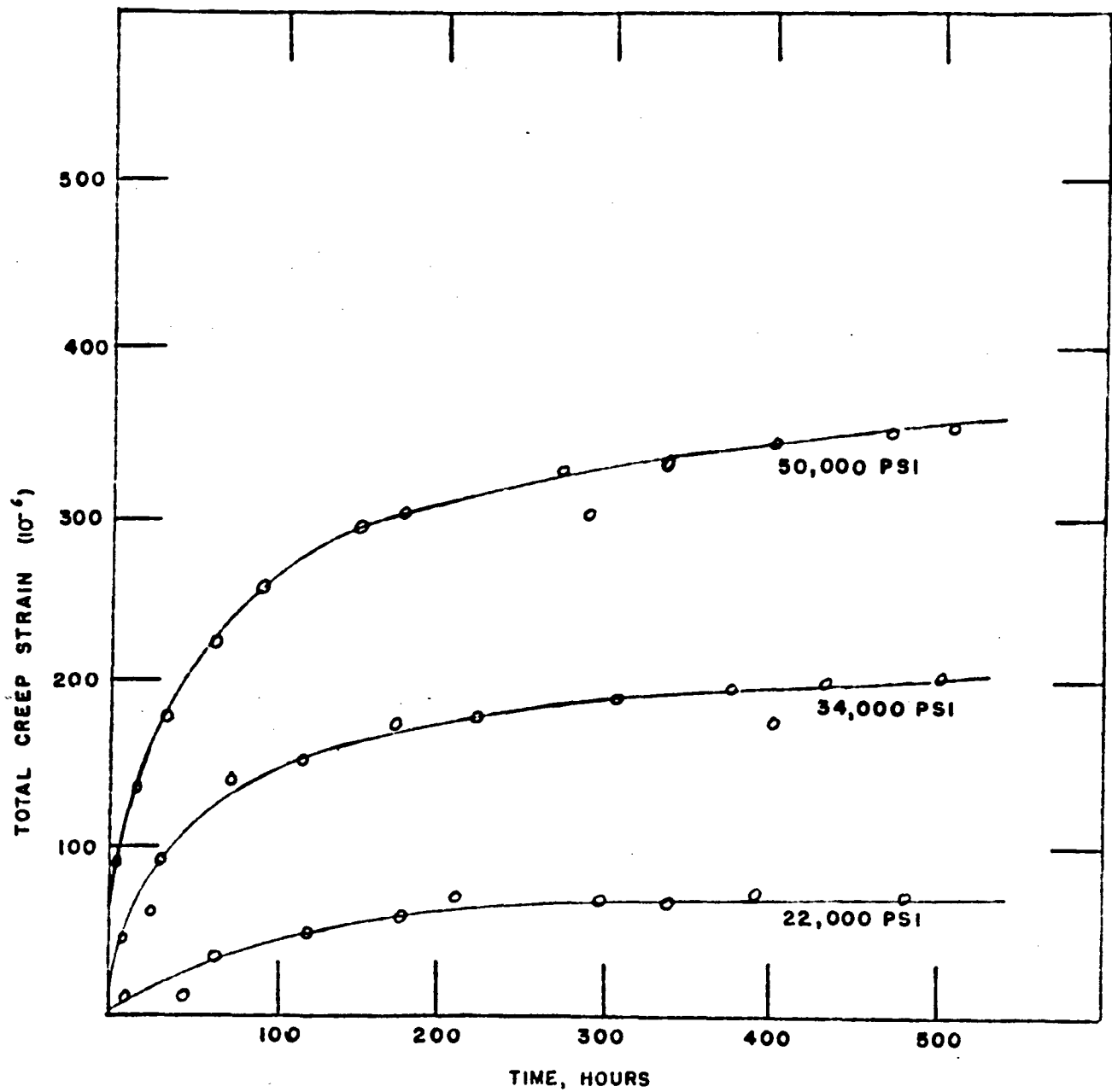


Figure 14 - Total Creep Curves of Invar "50" at 500°F.



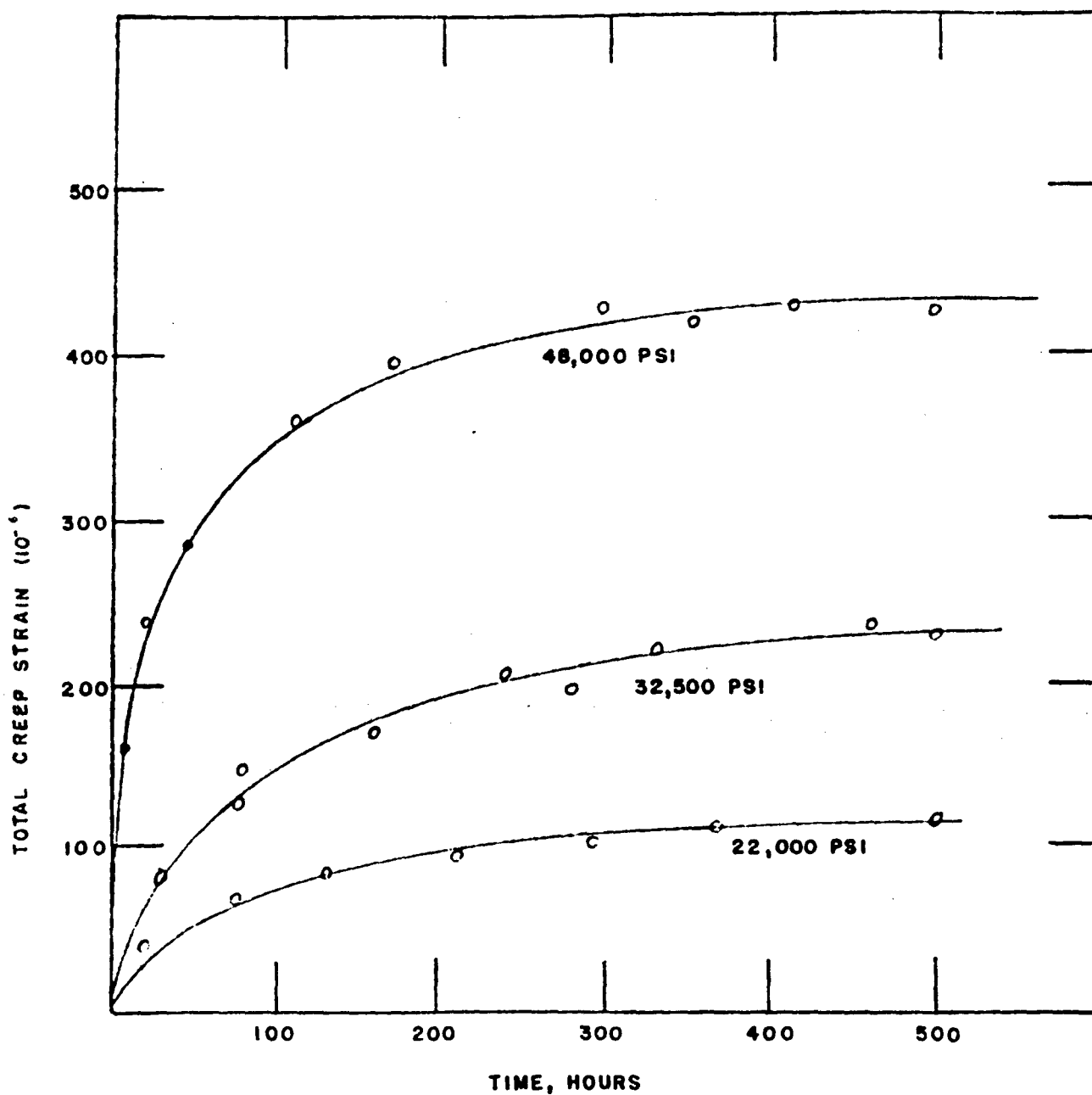


Figure 1 - Total creep curves of Invar "36" at 15°F

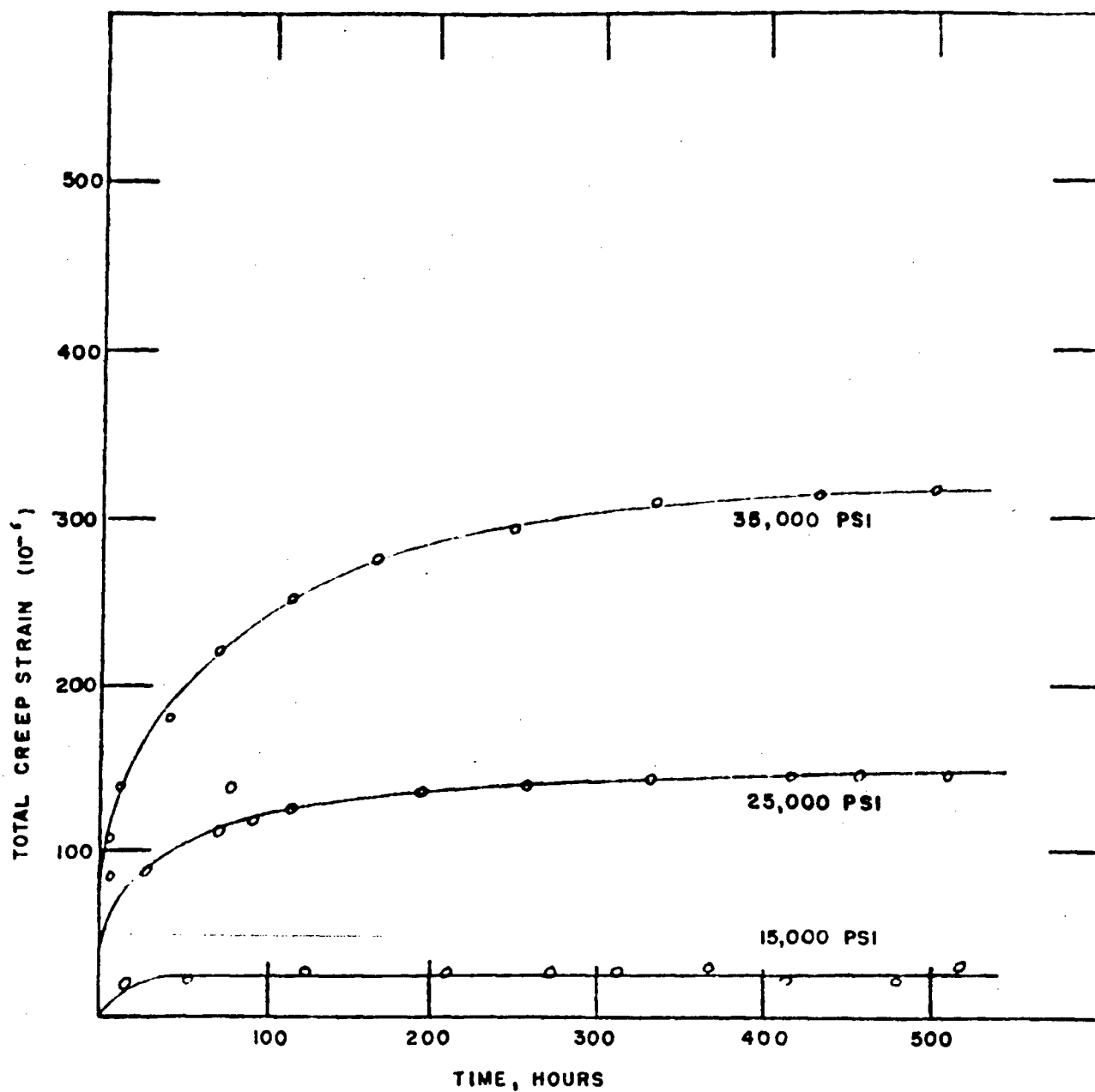


Figure 14 - Total Creep curves of Invar "46" at 100°F.

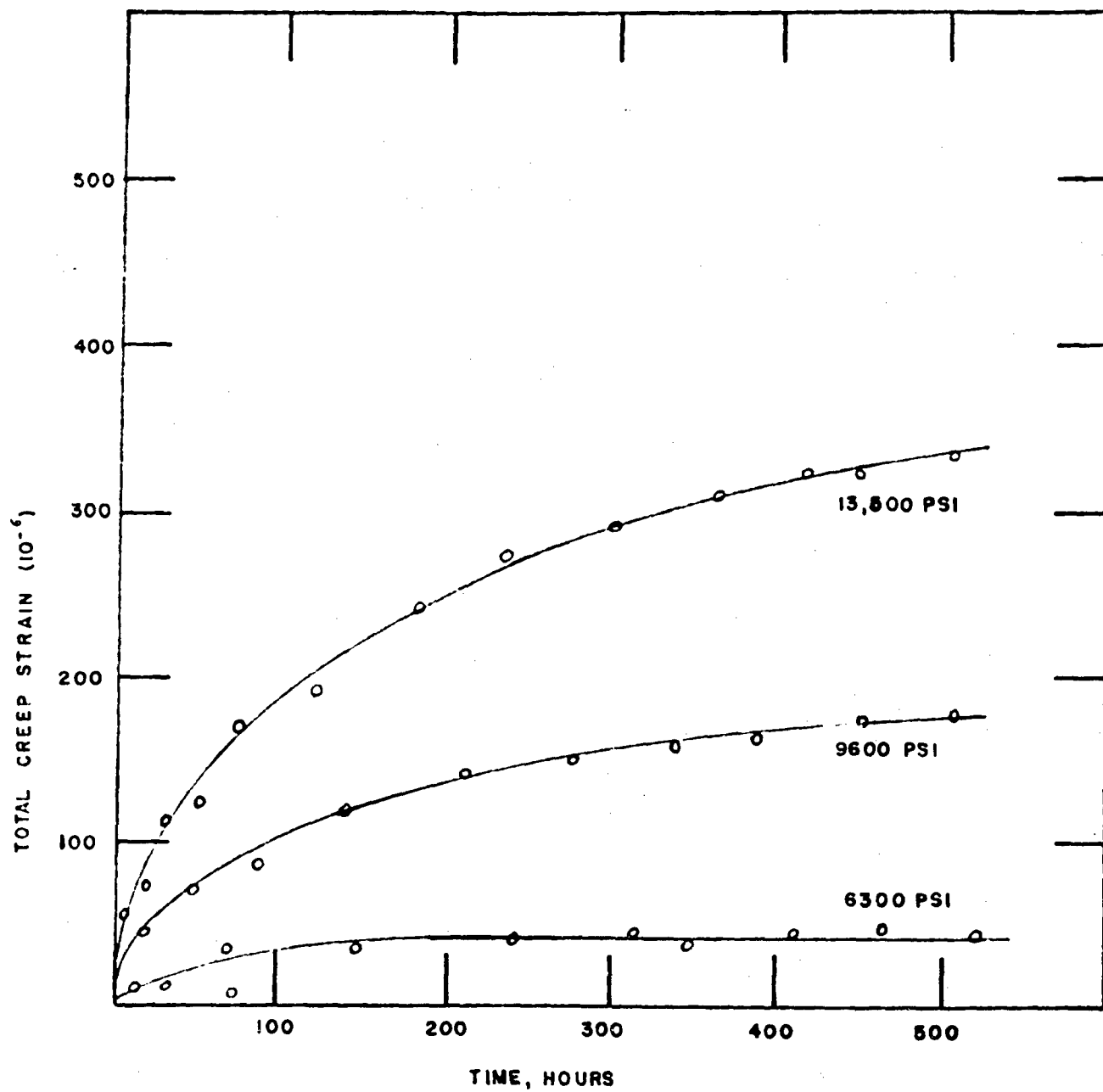


Figure 15 - Total Creep curves of 505-T6 Aluminum at 85°F.

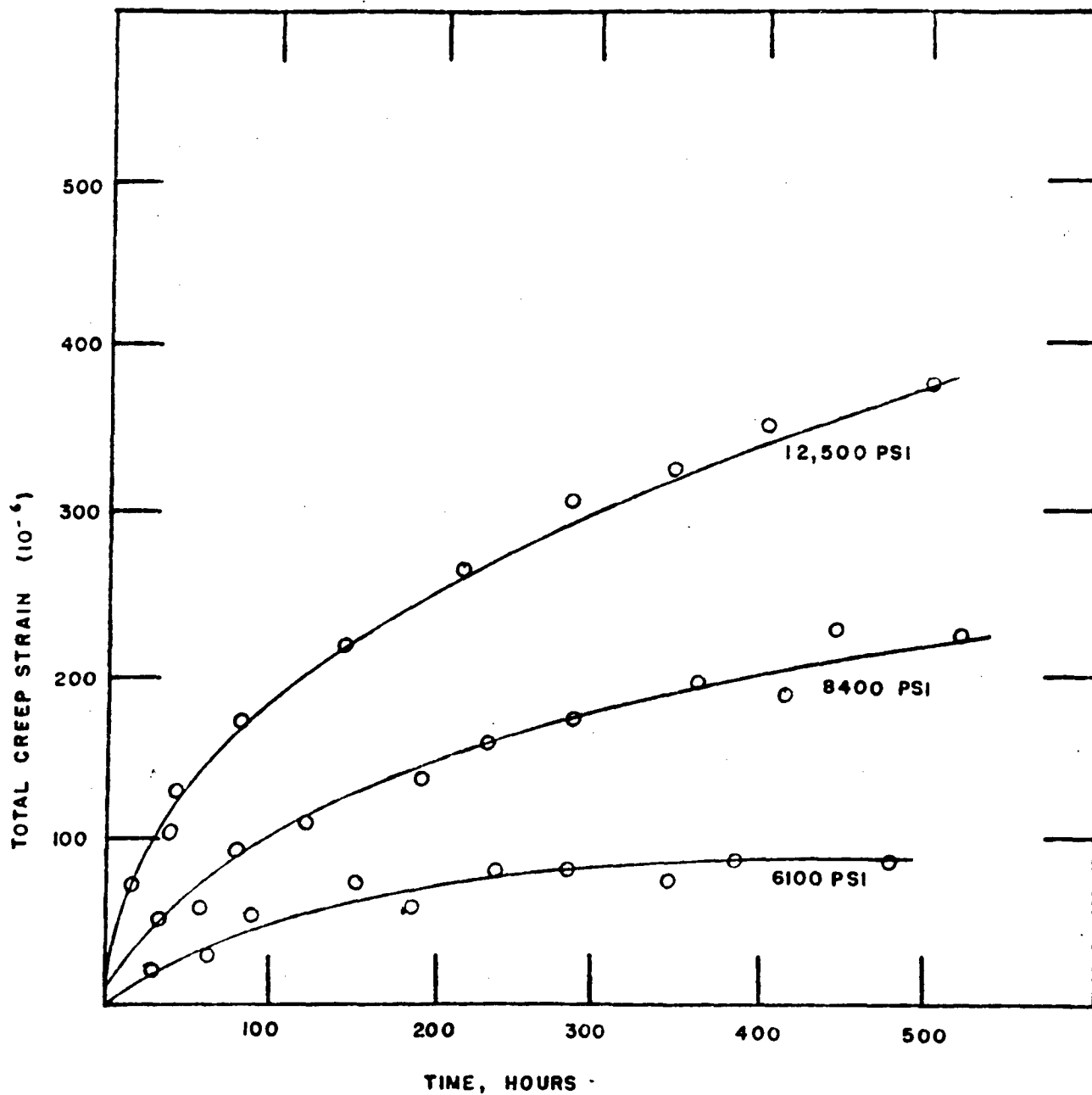


Figure 16 - Total creep curves of 2024-T3 Aluminum at 100°F.

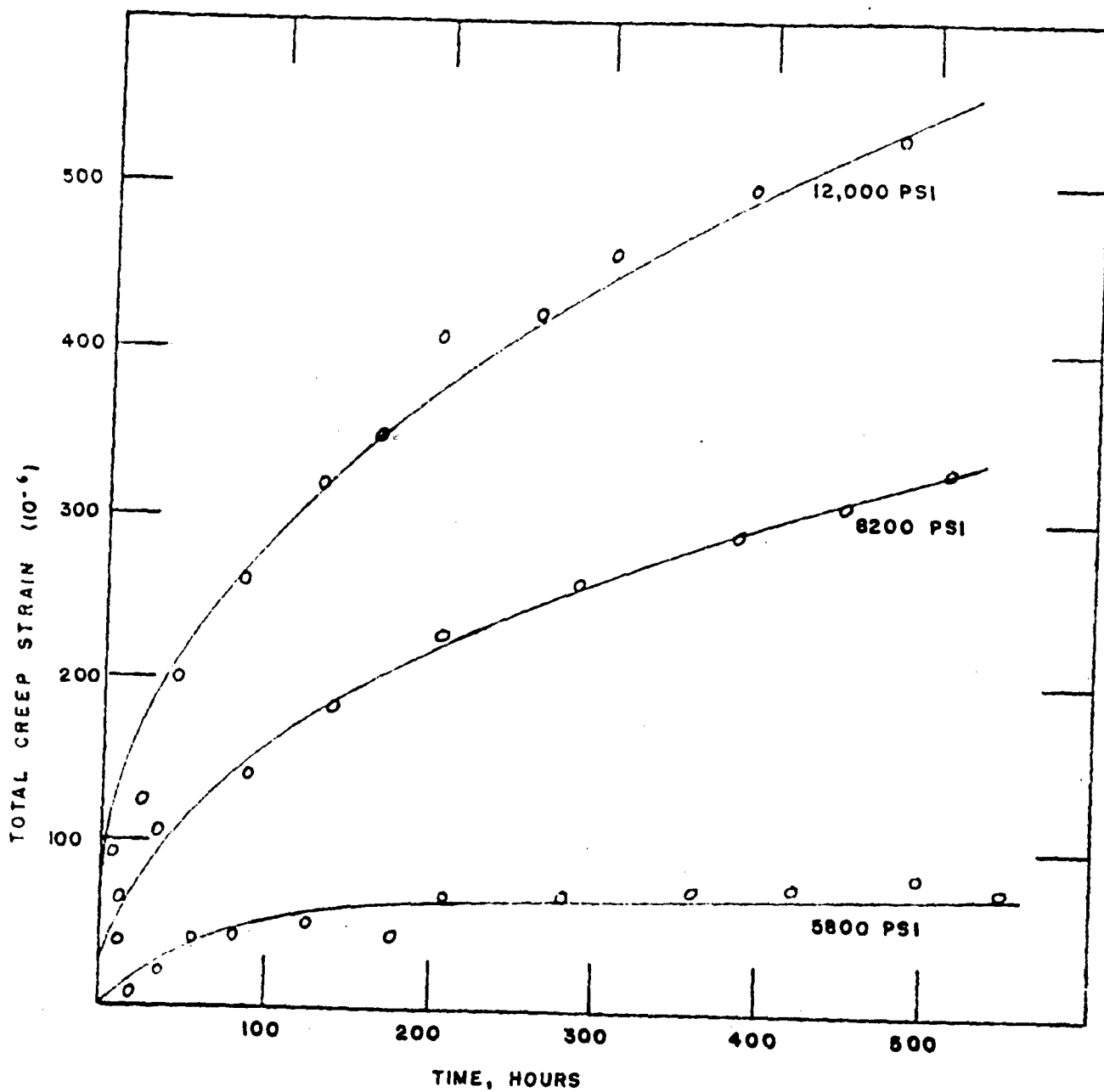


Figure 17 - Total creep curves of 2024-T3 Aluminum at 200°F.

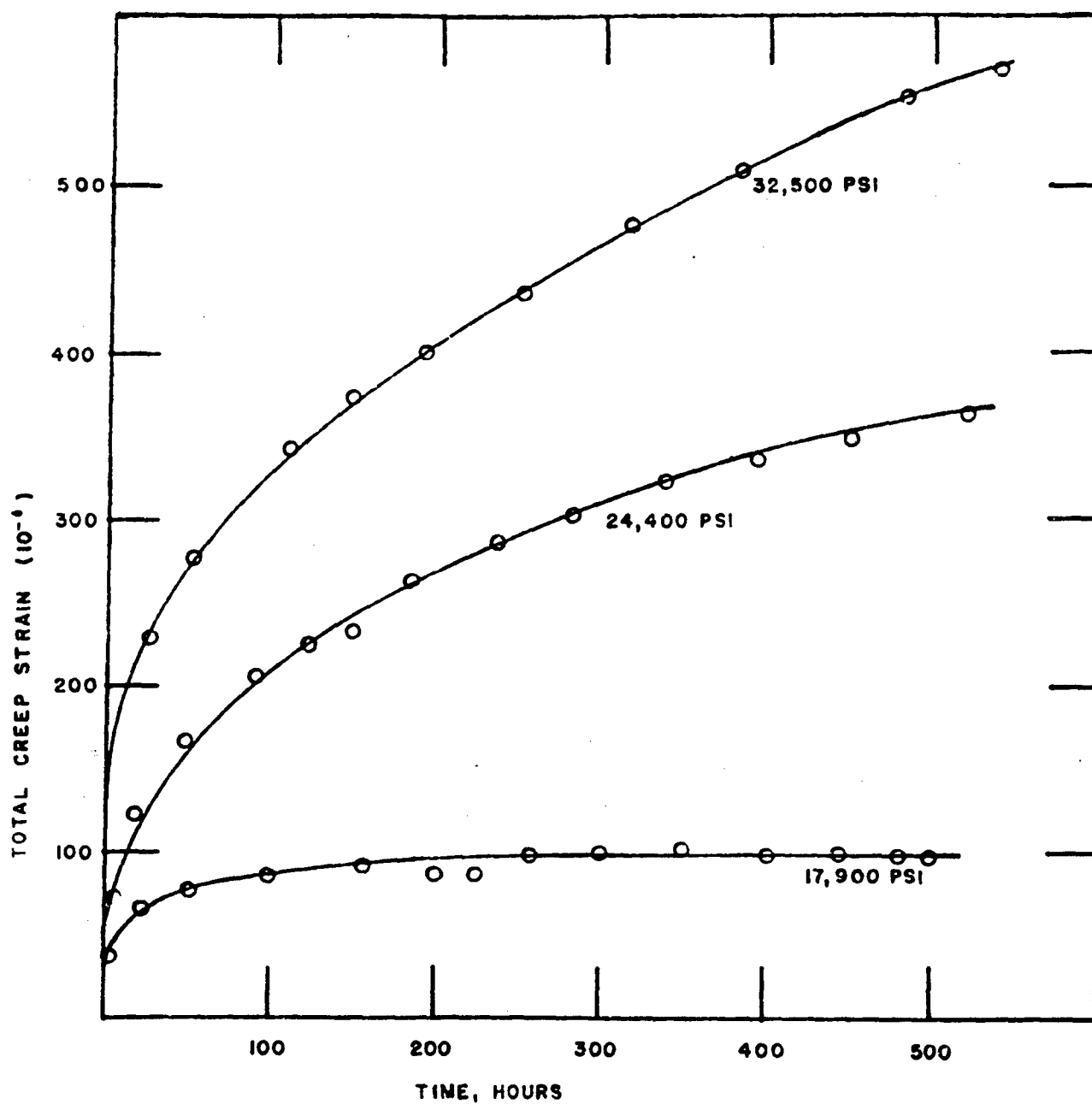


Figure 18 - Total creep curves of 316 stainless steel at 500°F.

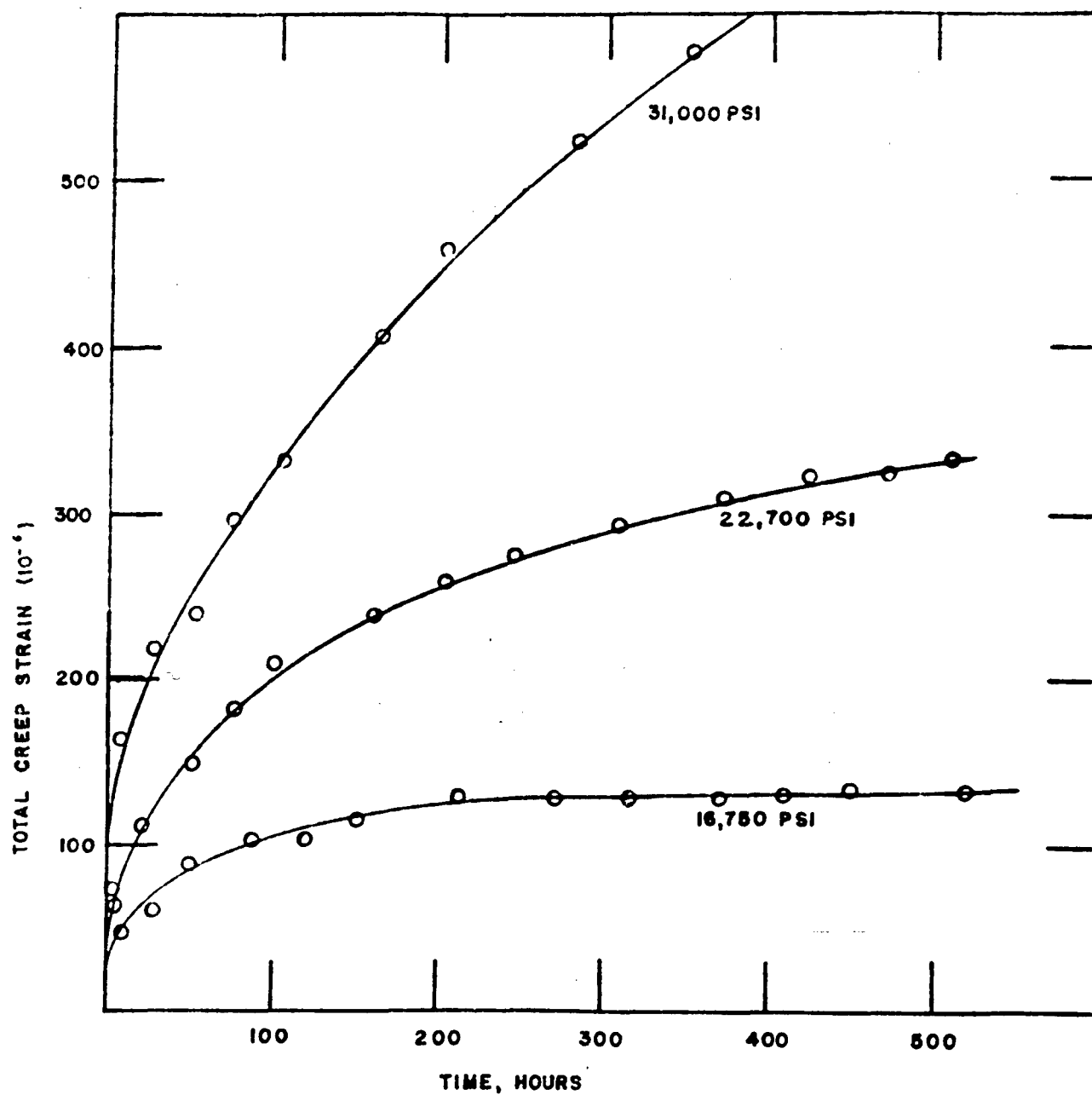


Figure 14 - Total creep curves of 316 stainless steel at 150°F.

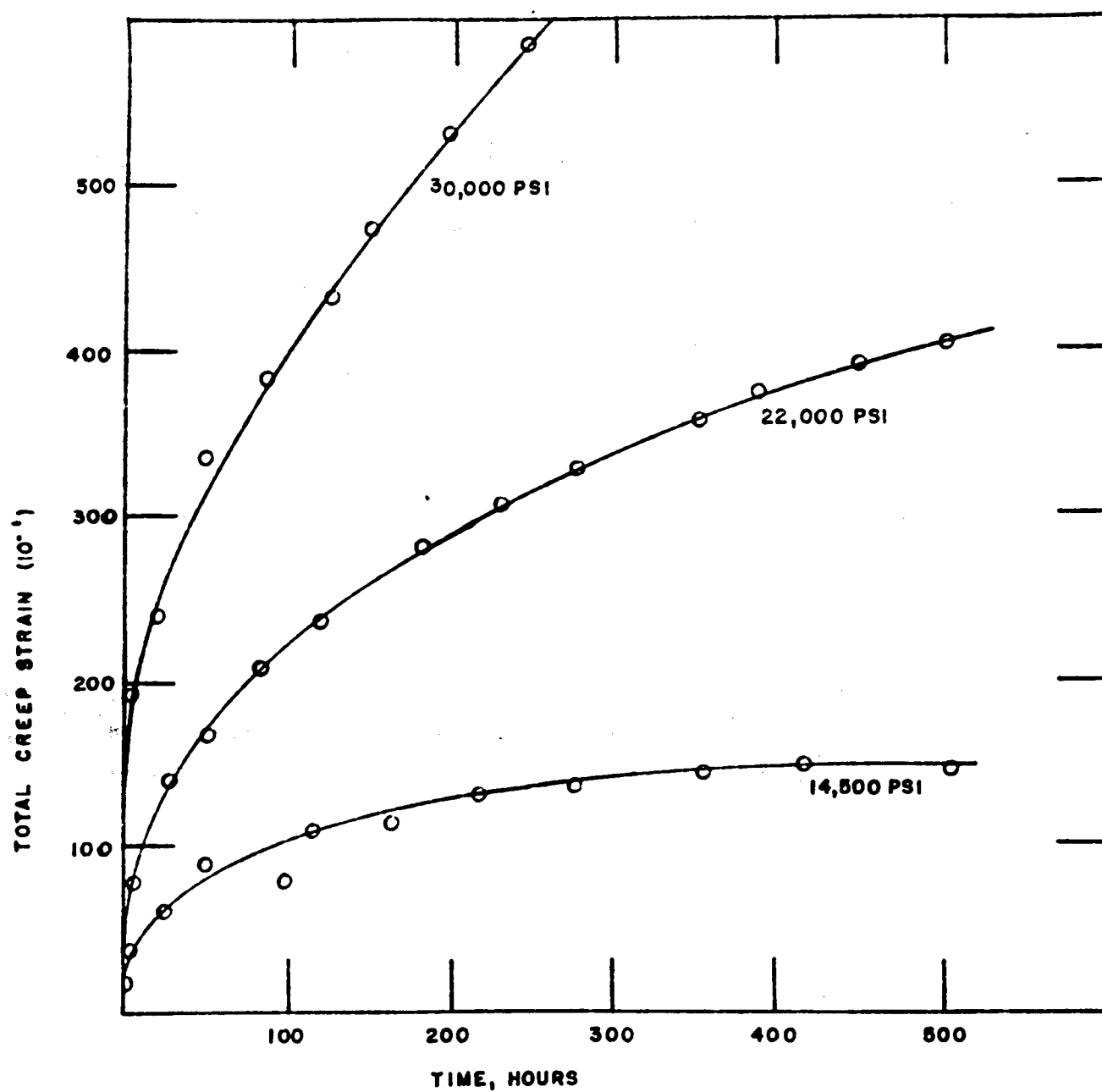


Figure 20 - Total creep curves of 316 stainless steel at 1000°F.



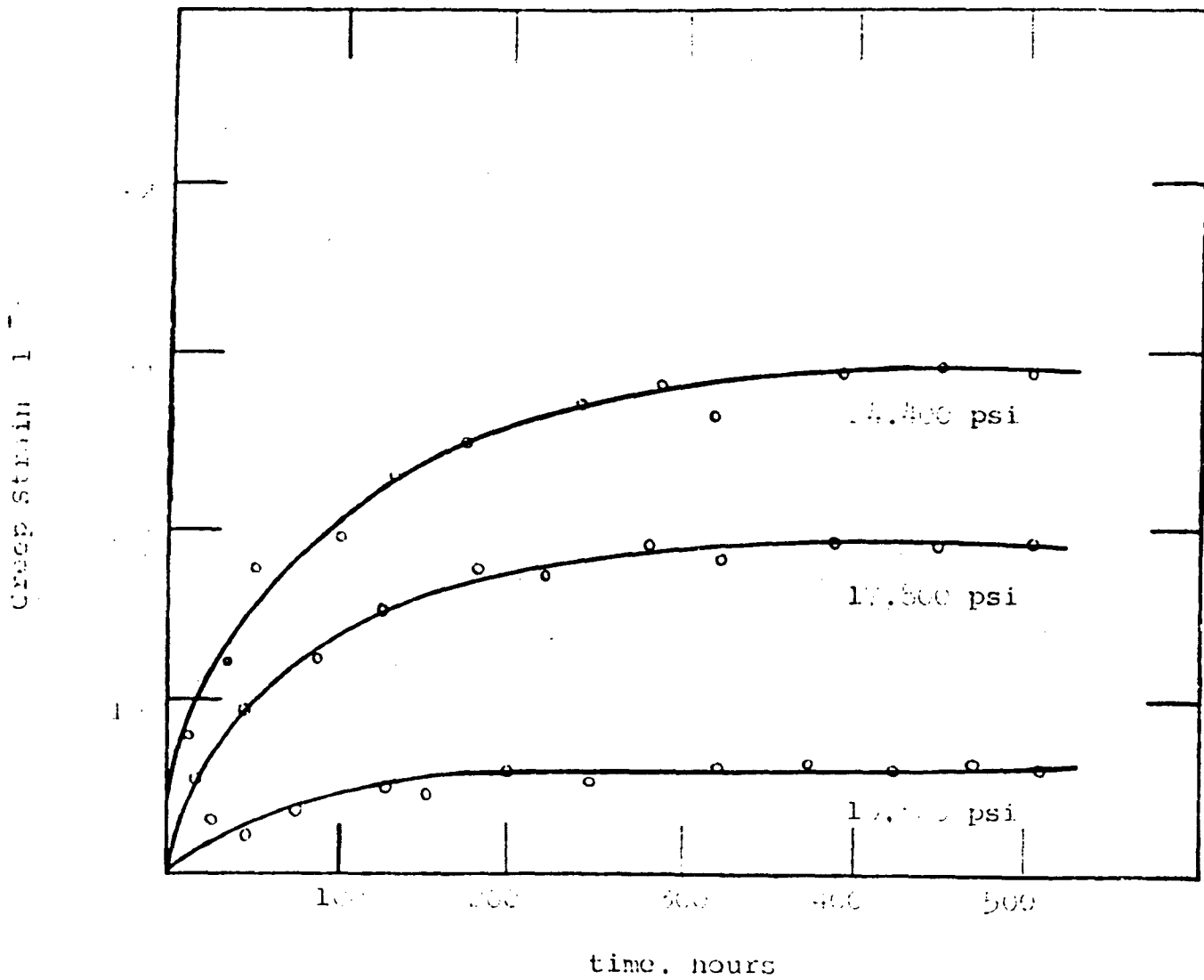


Figure 21 - Total creep curves of 6061-T6 aluminum at 85°F.

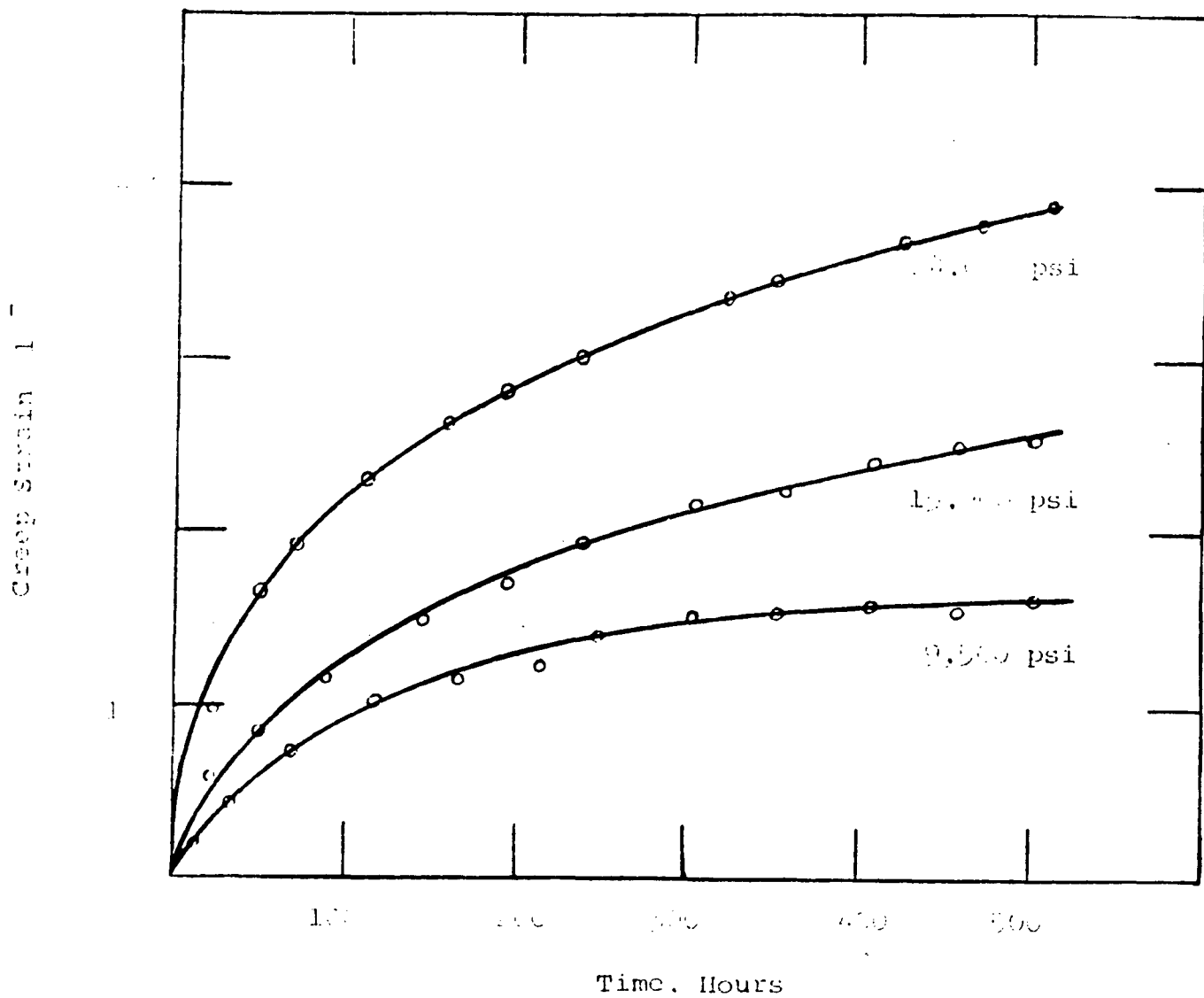


Figure 22 - Total creep curves of 6061-T6 aluminum at 150°F.

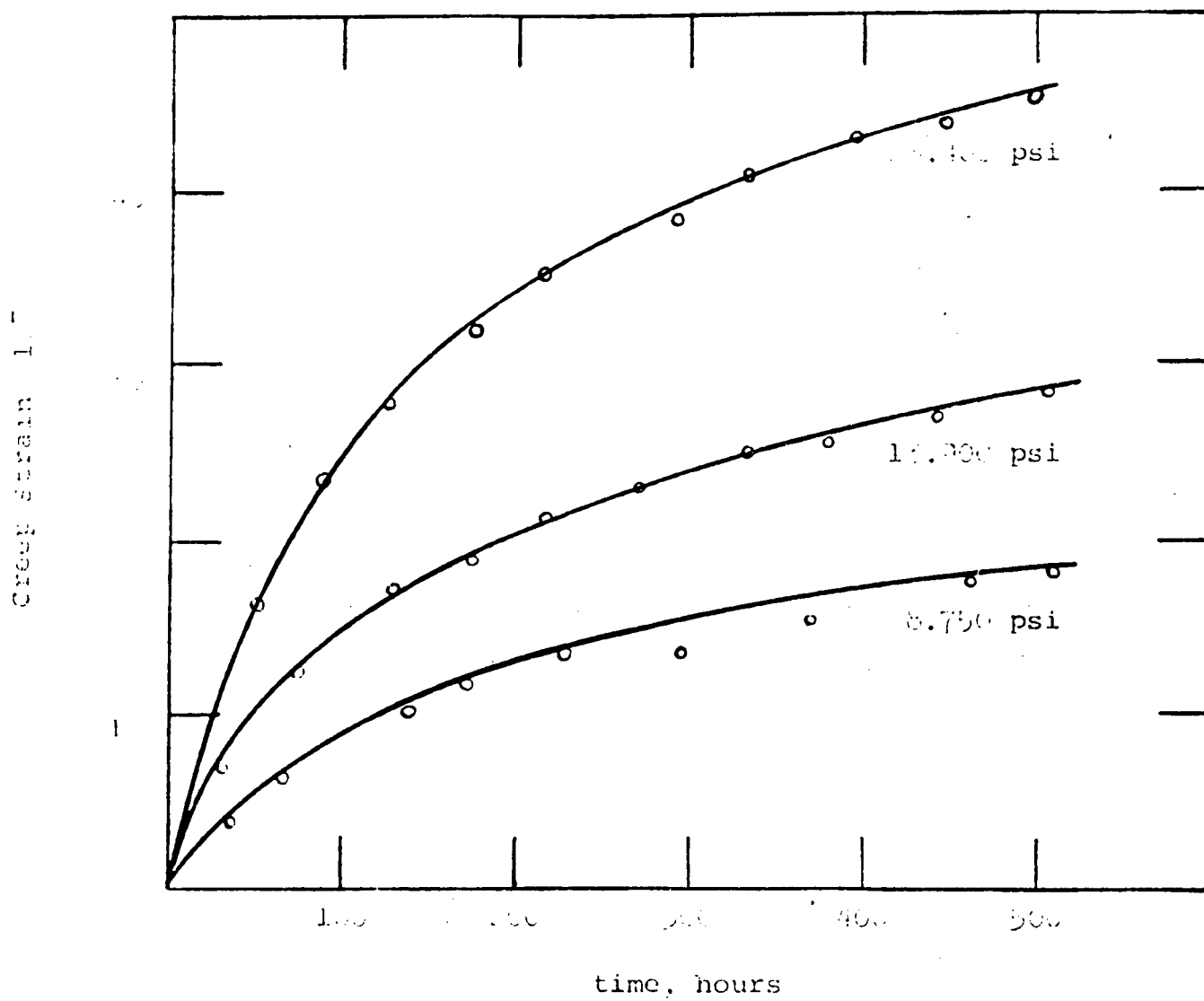


Figure 23 - Total creep curves of 6061-T6 aluminum at 200°F.

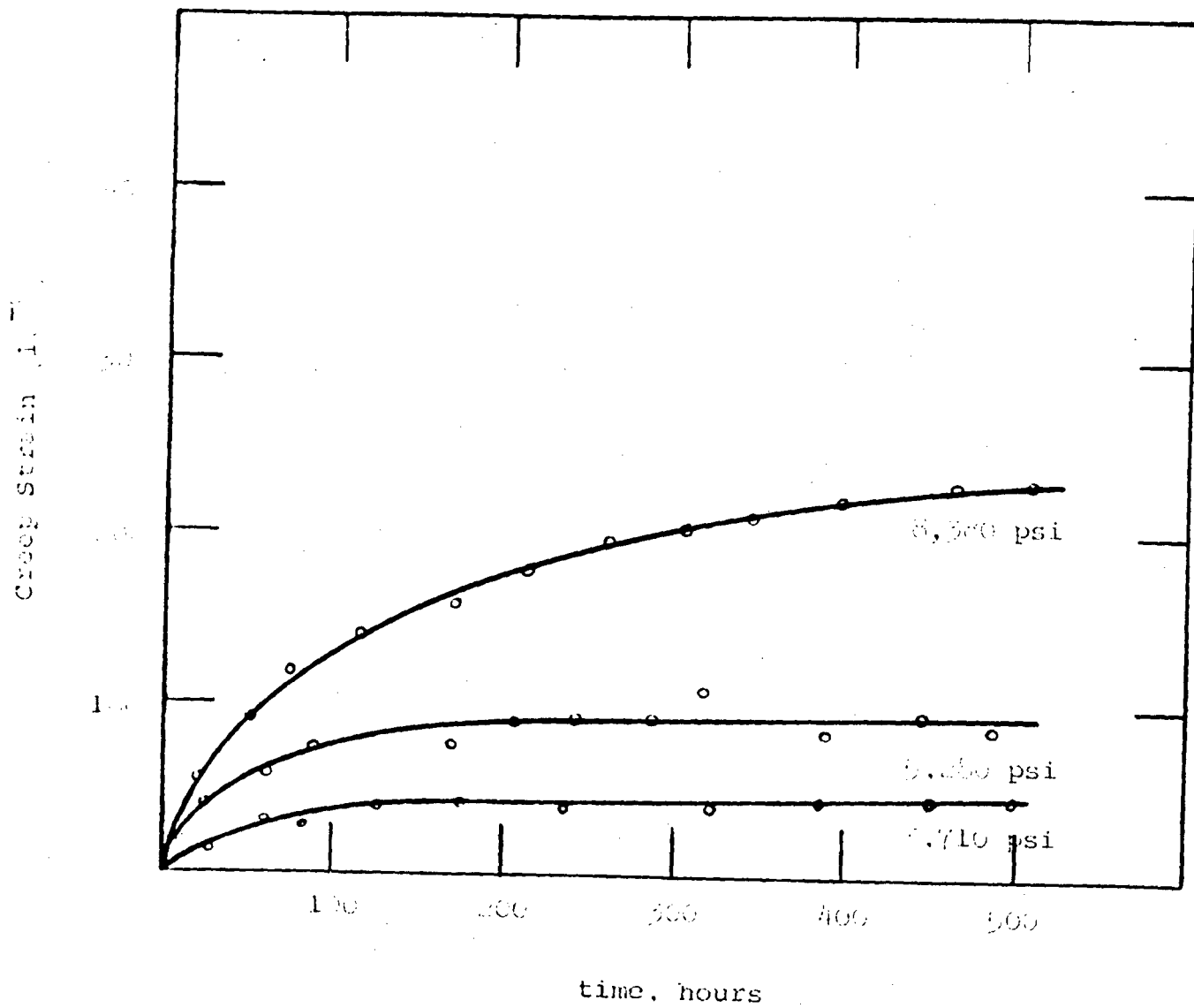


Figure 24 - Total creep curves of AZ31A magnesium at 85°F.

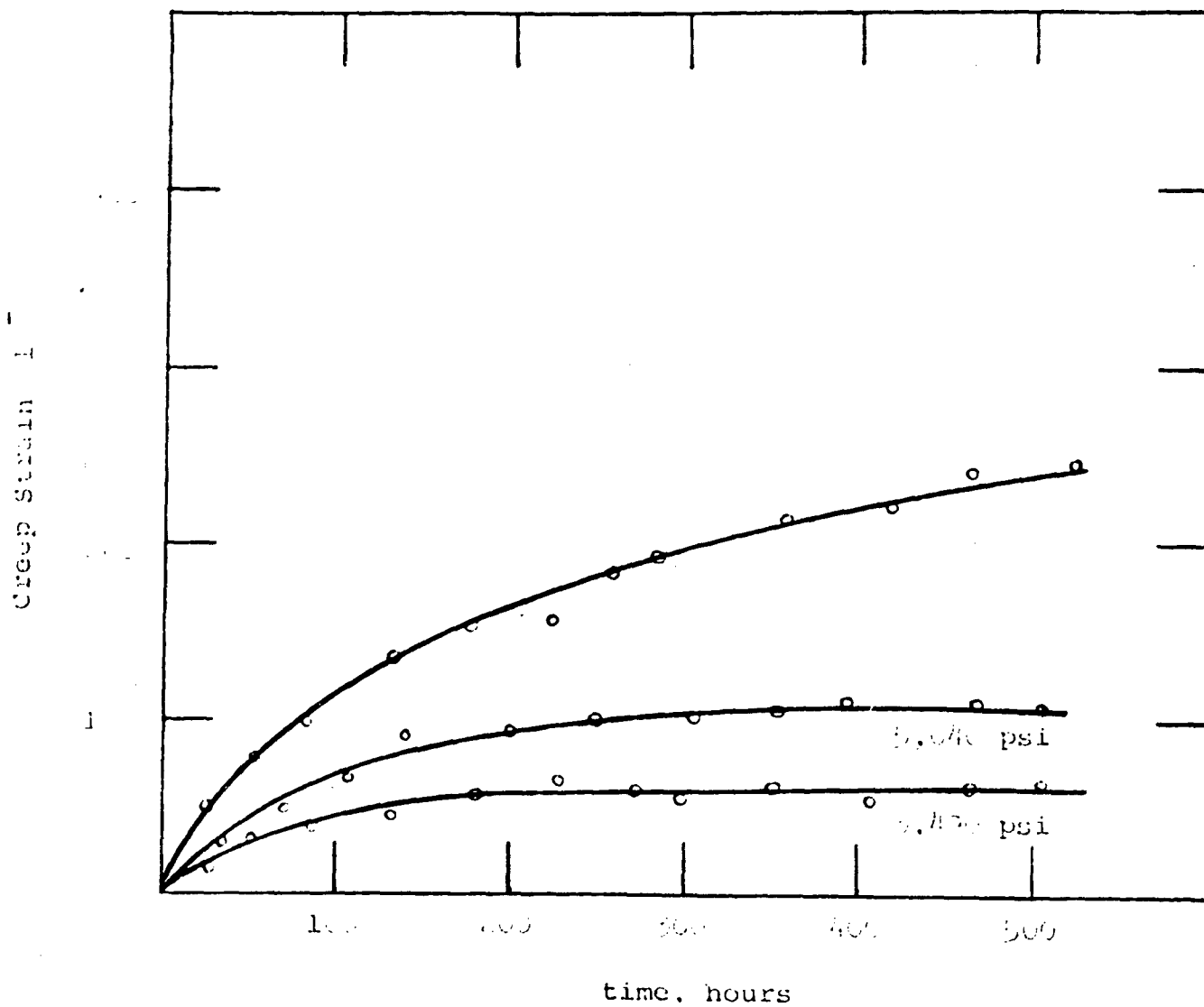


Figure 25 - Total creep curves of AZ92A magnesium at 150°F.

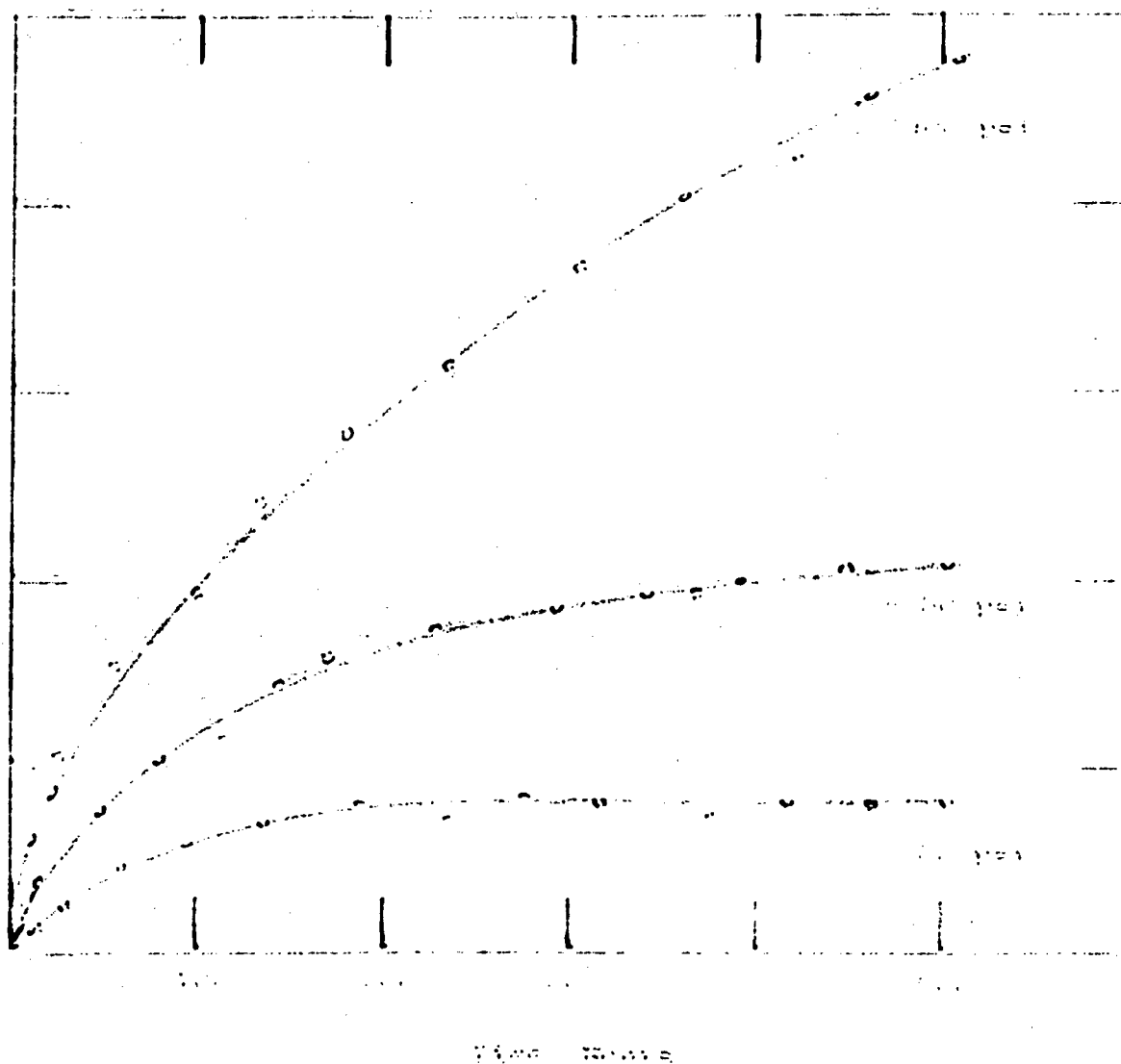


Figure 10 - Total yield curves of *Azolla macrospora* at 20°C.

creep rate decreases to a constant or steady state condition (second stage) which is followed by an increasing creep rate (tertiary creep) until failure occurs.

To explain creep behavior in the first or transient stage two mechanisms have been advanced. Considering the rate determining mechanism at low temperatures as the motion of dislocations through a forest of dislocations b, the creation of jogs leads to the well known logarithmic creep law<sup>(7)</sup> given by:

$$\epsilon \sim k \log t \quad (1)$$

At higher temperatures where the dislocations can acquire enough thermal energy to climb and thereby avoid obstacles, analysis gives the Andrade relationship.<sup>(8)</sup>

$$\epsilon \sim \beta t^{1/3} \quad (2)$$

which is known as the  $\beta$ -creep law.

Both these mechanisms assume a large degree of cold work prior to creep in order to create the forest of dislocations. However, it has been recently demonstrated that although well defined deformation occurs in the micro-yield region, the dislocations are not extensive enough

to form extensive forests. (9) Thus, at stress below and slightly above the elastic limit the  $\dot{\epsilon}$  and logarithmic creep laws are not expected to be strictly valid.

It has been demonstrated that in the region of the  $10^{-6}$  or  $10^{-7}$  elastic limit, permanent plastic deformation takes place by the multiplication and motion of pinned dislocations and that this mechanism is thermally activated. (3,4) With the application of a stress in the region of the elastic limit, dislocations bow out creating new dislocations which move until obstacles are met. The dislocation multiplication ceases when the back stress from the blocked dislocations stops the operation of the source. This is the state when microcreep begins.

Since the average sources active at the constant stress level have been exhausted further deformation can only be accomplished by activating more dislocation sources or by re-activating the exhausted sources. It is assumed that this occurs when a fluctuation of the internal stress aided by thermal activation takes place.

The creep rate for this process is given by

$$\frac{d\epsilon}{dt} = n A b \frac{\dot{\epsilon}}{n} \quad (3)$$



where  $N$  is the number of dislocation loops per square centimeter,  $A$  is the area of active slip planes in the specimen,  $b$  the burger's vector,  $\dot{N}$  is the rate of multiplication of dislocations, and  $n$  is the number of fluctuations necessary to build up to the minimum stress to activate a dislocation source. If we assume that random stress fluctuations take place with a mean square distribution around the applied stress  $\sigma_a$ , then:

$$n = \frac{\Delta\sigma^2}{\sigma_a^2} \quad n = \left( \frac{\Delta\sigma}{\sigma_a} \right)^2 \quad (4)$$

From the stress-plastic strain curves of Figure 11, at stress levels above the elastic limit and stress fluctuation is given by:

$$\Delta\sigma = K\epsilon^{1/2} \quad (5)$$

However, since the creep curves represent total creep rather than the plastic component of total creep, the stress fluctuations may not be defined by the plastic strain curves but should fall nearer the stress-total strain curves. Writing the stress fluctuation as

$$\Delta\sigma = K_0 \epsilon^n \quad (6)$$

where  $0 \leq m \leq 1$ ,

equation 3 becomes

$$\frac{d\epsilon}{dt} = \frac{NAb}{K_0 \epsilon} \frac{\sigma^2}{2m} \quad (7)$$

which integrates to

$$\epsilon = (2m+1) \left( \frac{NAb}{K_0 \epsilon} \right) \frac{1}{2m+1} (\sigma^2 t) \frac{1}{2m+1} \quad (8)$$

or

$$\epsilon = K_1 (\sigma^2 t) \frac{1}{2m+1} \quad (9)$$

For the parabolic stress dependence,  $m = 1/2$  and Eq. (9) reduces to  $\epsilon = K_1 \sigma (t)^{1/2}$ . The difference between the cube root time dependence of  $\beta$ -creep and the parabolic time dependence of equation 7 arises from the value of the stress fluctuations which in the  $\beta$ -creep derivation were assumed to be directly proportional to the strain.

In the theory of  $\beta$ -creep the rate of dislocation multiplication is replaced by the rate of dislocation climb. To evaluate we must evaluate

the probability of creating a mobile dislocation. It has been demonstrated that this process takes place when an unpinned length of dislocation bows out to an unstable size where its radius of curvature reaches half the original pinned dislocation length. Furthermore, this process is thermally activated and aided by the internal stress. Denoting the activation energy as  $Q$ , the activation probability for dislocation multiplication in the forward direction is given by:

$$P_f \sim \exp \frac{-Q - (\sigma - \sigma_0)b^2}{kT} \quad (10)$$

where  $\sigma_0$  is the critical stress necessary to activate the average dislocation source. In the reverse direction, the expression is:

$$P_r \sim \exp \frac{-Q + (\sigma - \sigma_0)b^2}{kT} \quad (11)$$

Since the rate of dislocation multiplication is given by the product of the number of attempts to climb the energy barrier and the probability of overcoming the barrier, adding equations 10 and 11 gives the net rate of dislocation multiplication as:

$$\dot{\epsilon} = n\nu \sinh \left( \frac{(\sigma_a - \sigma_0)b^2}{kT} \right) \exp(-Q/kT) \quad (12)$$

where  $n$  is the number of sources and  $\nu$  the vibration frequency of the dislocation line. Combining equations 9 and 12 yields a final expression for the creep strain above the  $10^{-6}$  elastic limit stress of

$$\epsilon = K_1 \left( n\nu \sigma_a^2 t \sinh \left( \frac{(\sigma_a - \sigma_0)b^2}{kT} \right) \right)^{\frac{1}{2m+1}} \exp - \frac{Q}{(2m+1)kT} \quad (13)$$

or

$$\epsilon = K_2 \left( \sigma_a^2 t \sinh \left( \frac{(\sigma_a - \sigma_0)b^2}{kT} \right) \right)^{\frac{1}{2m+1}} \exp - \frac{Q}{(2m+1)kT} \quad (14)$$

In Figure 27-41 the creep curves are replotted on a logarithmic scale. The constants of equation 14 were calculated from the curves at stresses above the elastic limit and are tabulated in Table V. The values of  $\frac{1}{2m+1}$  are seen to vary between 1/3 and 1/2. The value of 1/2 results from a stress fluctuation defined by the stress-plastic strain curve and equation 5 while the 1/3 value would come from equation 6 with  $n = 1$ .

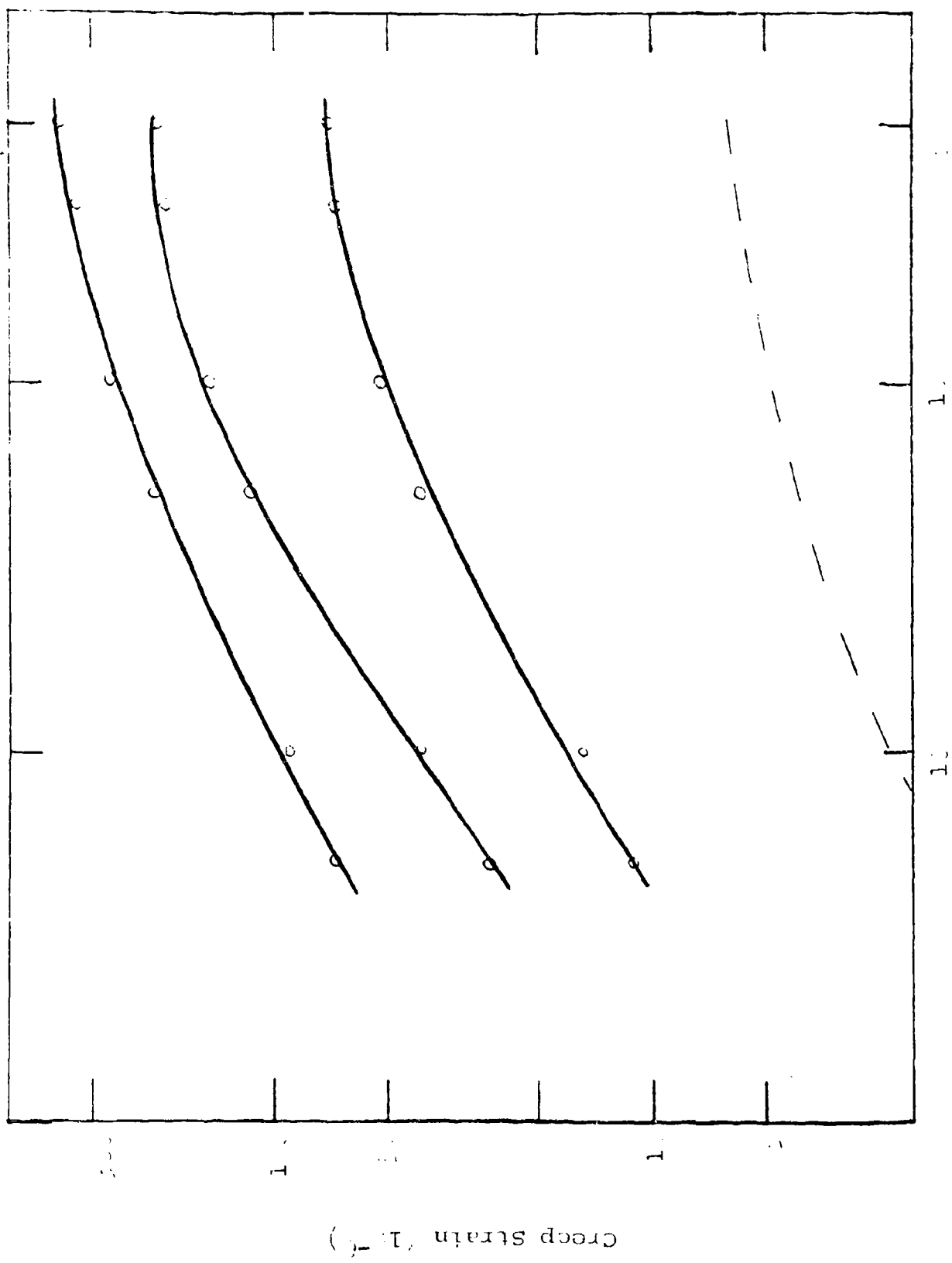


Figure 27 - Total creep curves of free cut invar at 1000 F.

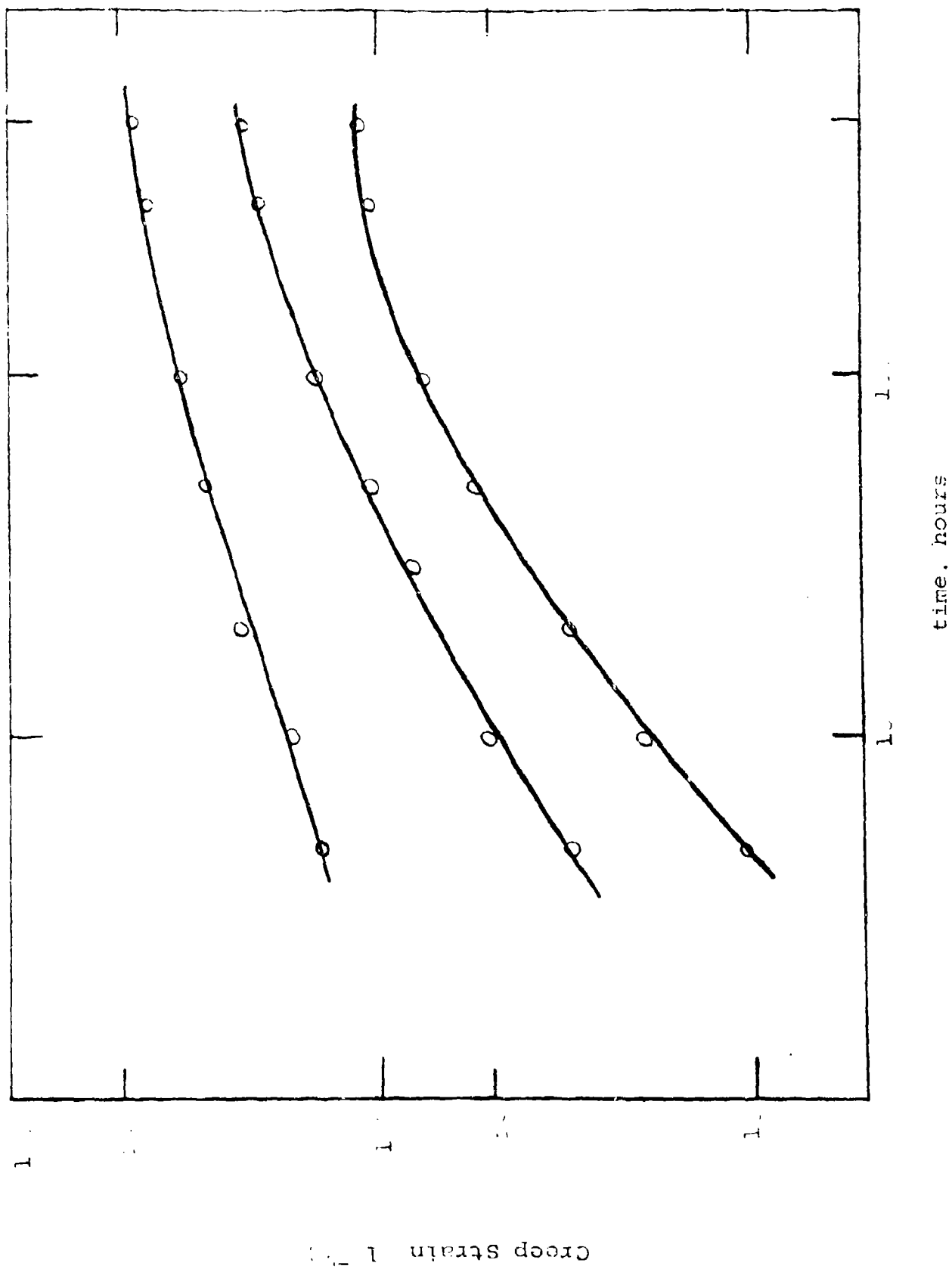


Figure 11 - Creep curves of free cut Invar at 100°F.

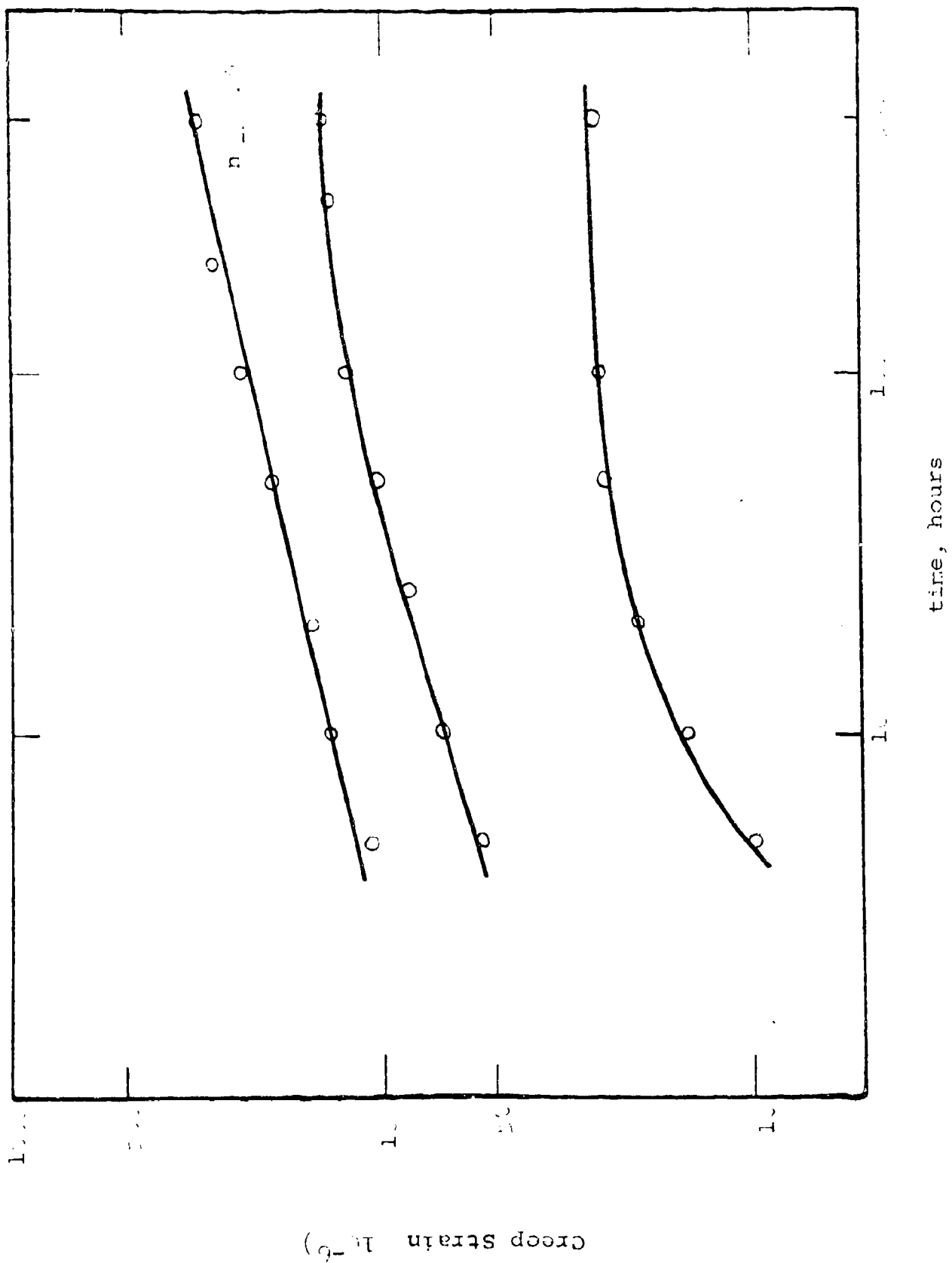


Figure 23 - Creep curves of free cut Inver at 211°F.

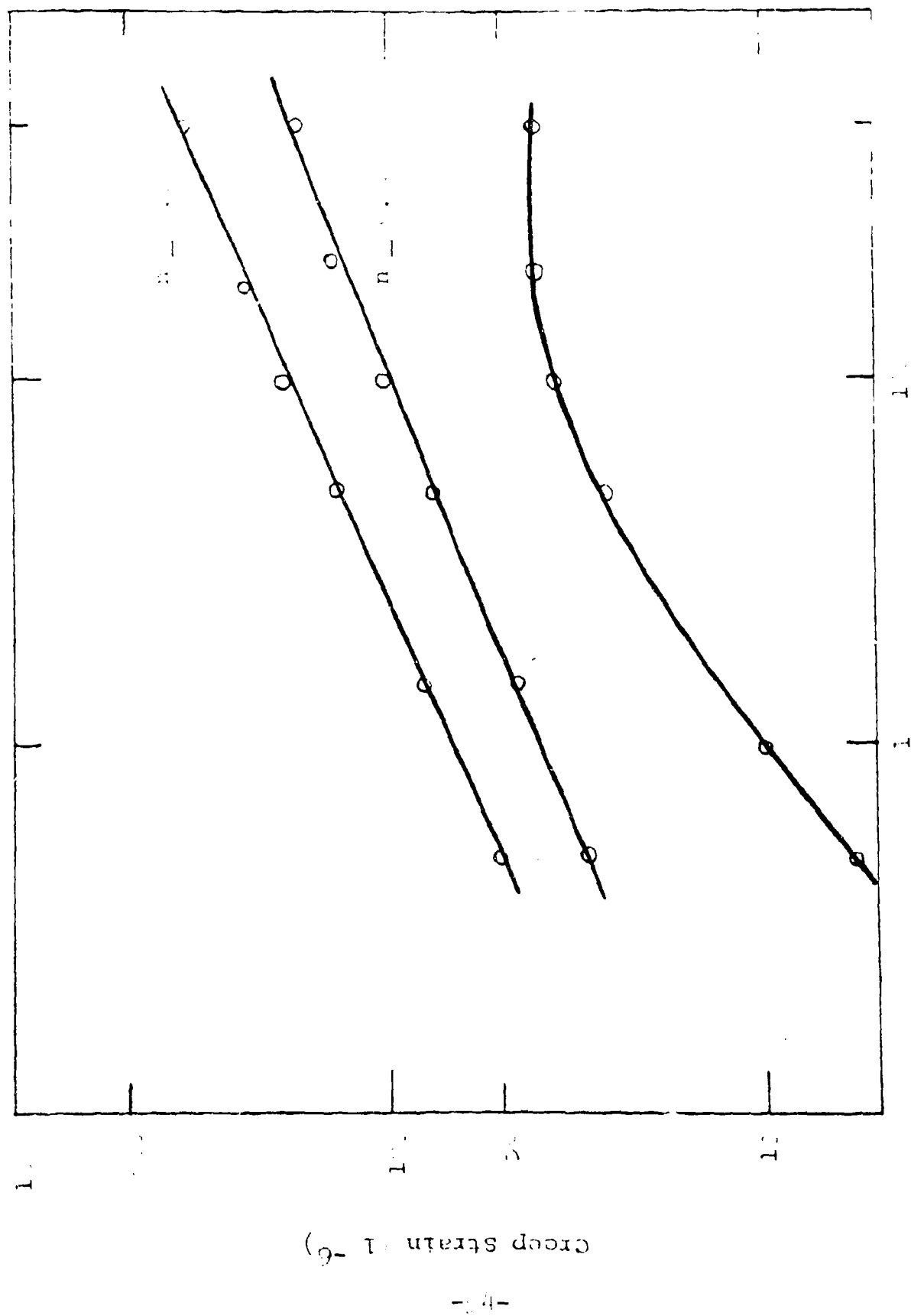


Figure 30 - Creep curves of 2024-T3 aluminum at 100°F.



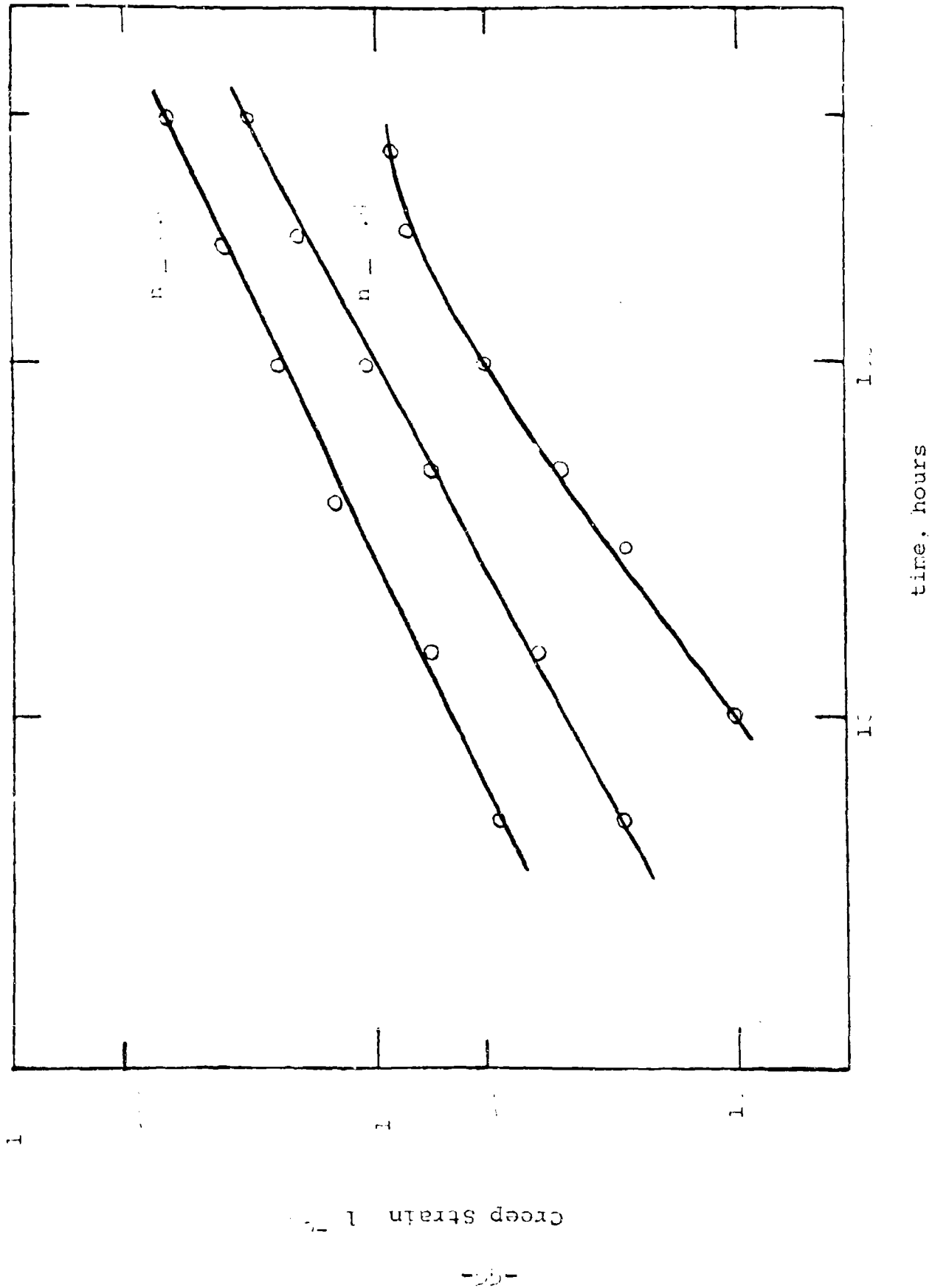


Figure 11 - Creep curves of 99.1-Tc aluminum at 1500 F.

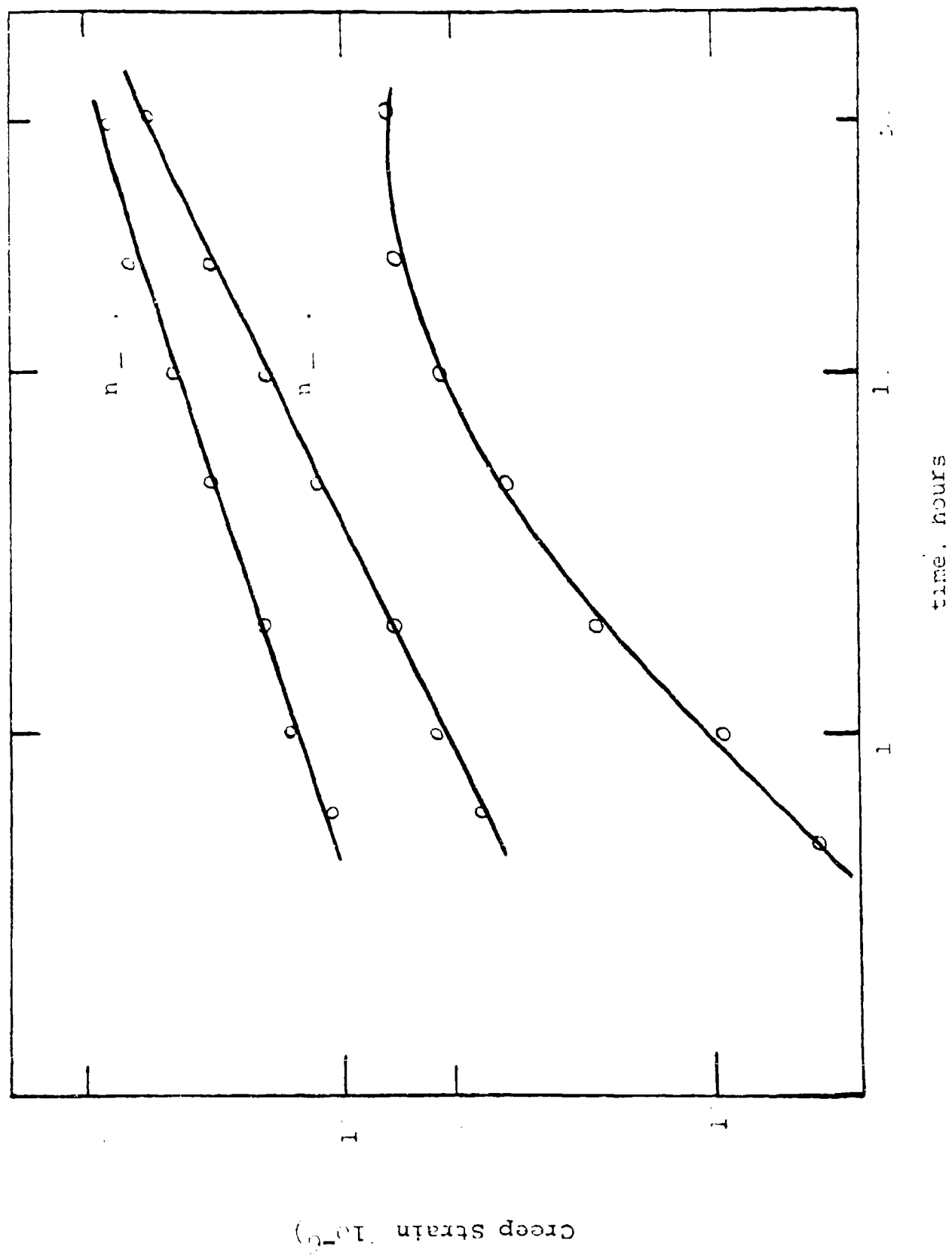


Figure 2 - Creep curves of 99.7% aluminum at 200°F.

Creep strain  $10^{-3}$

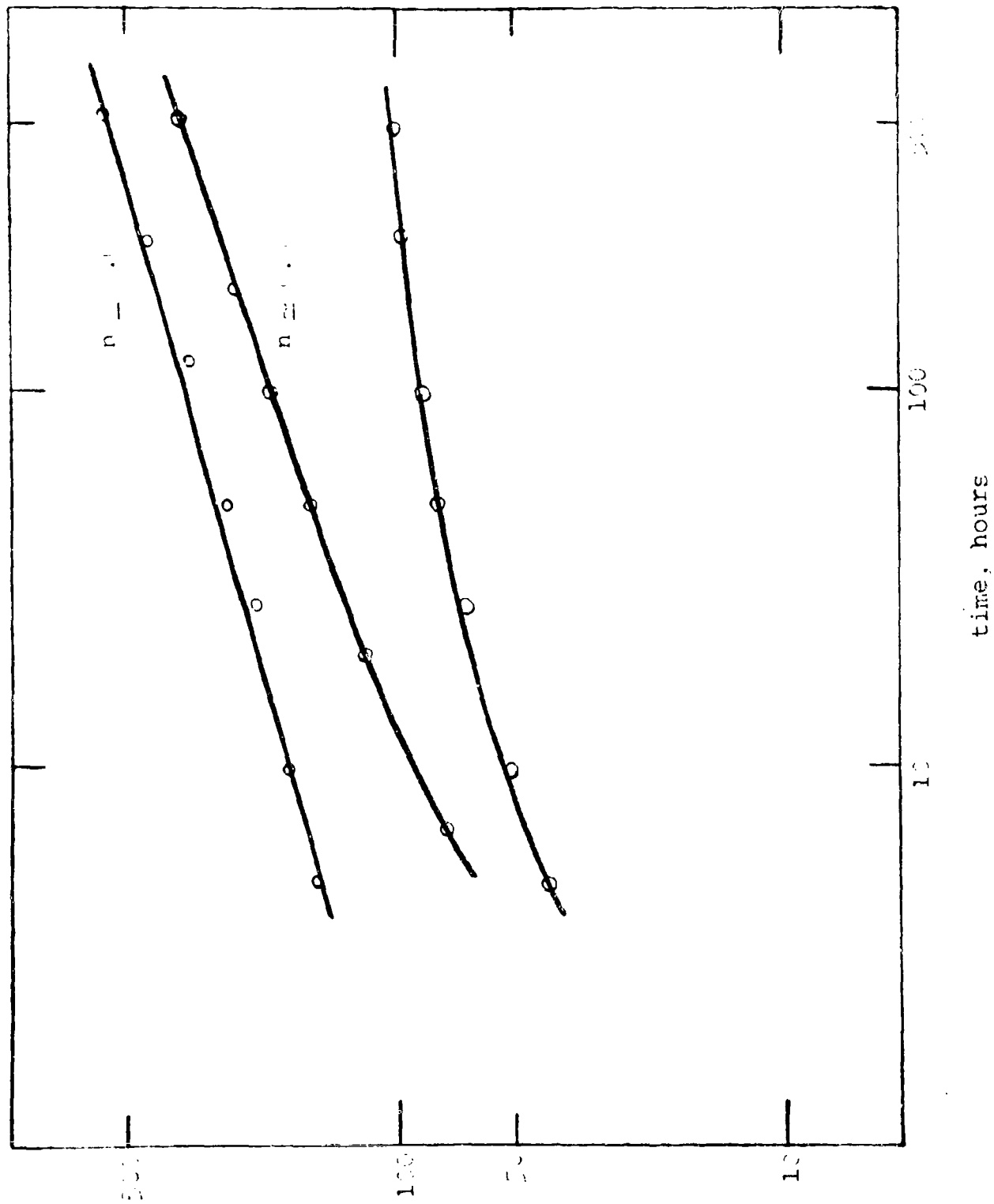


Figure 33 - Creep Curves of 71.5% nickel steel at 75°F.

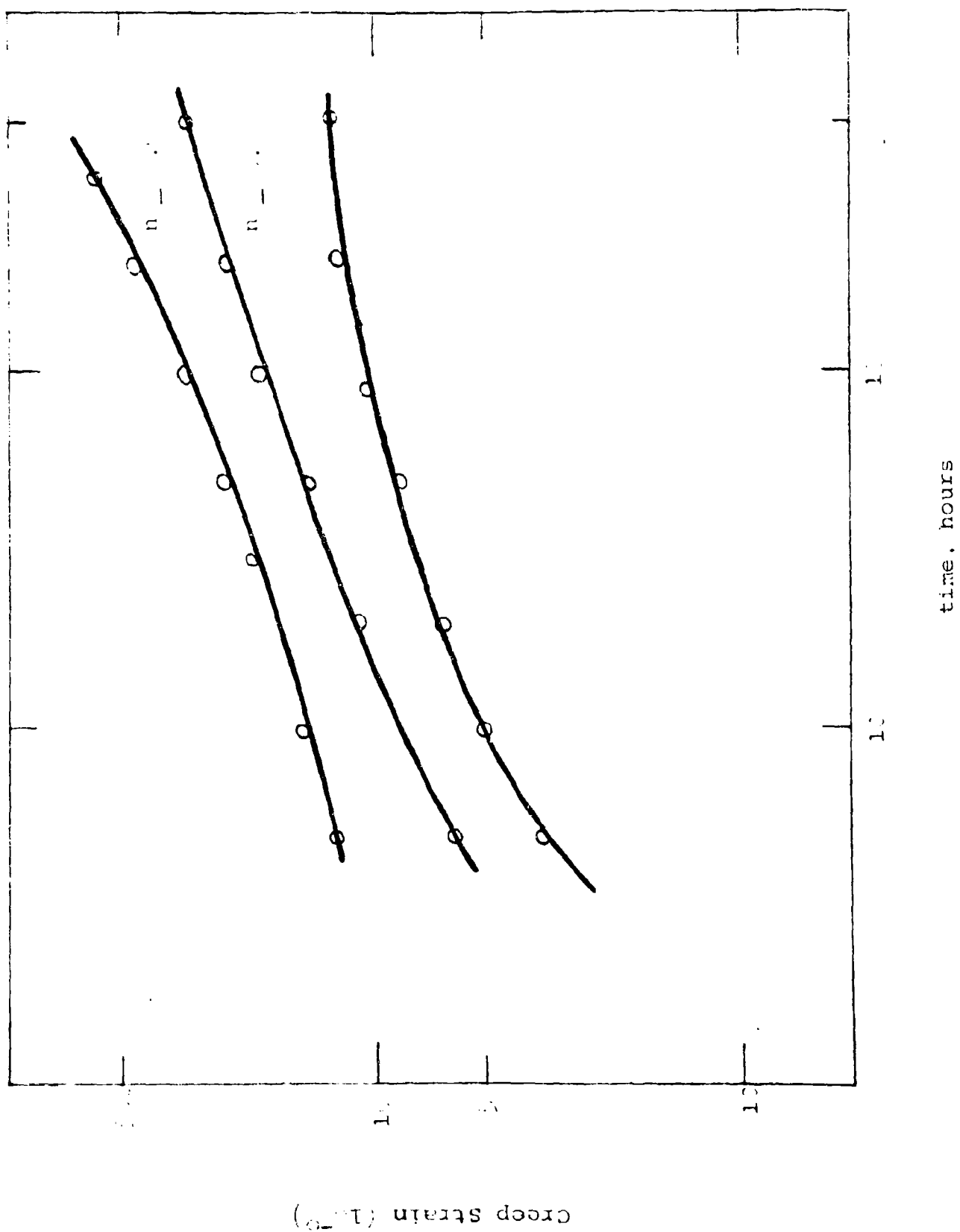


Figure 10 - Creep curves of 316 stainless steel at 1400°F.

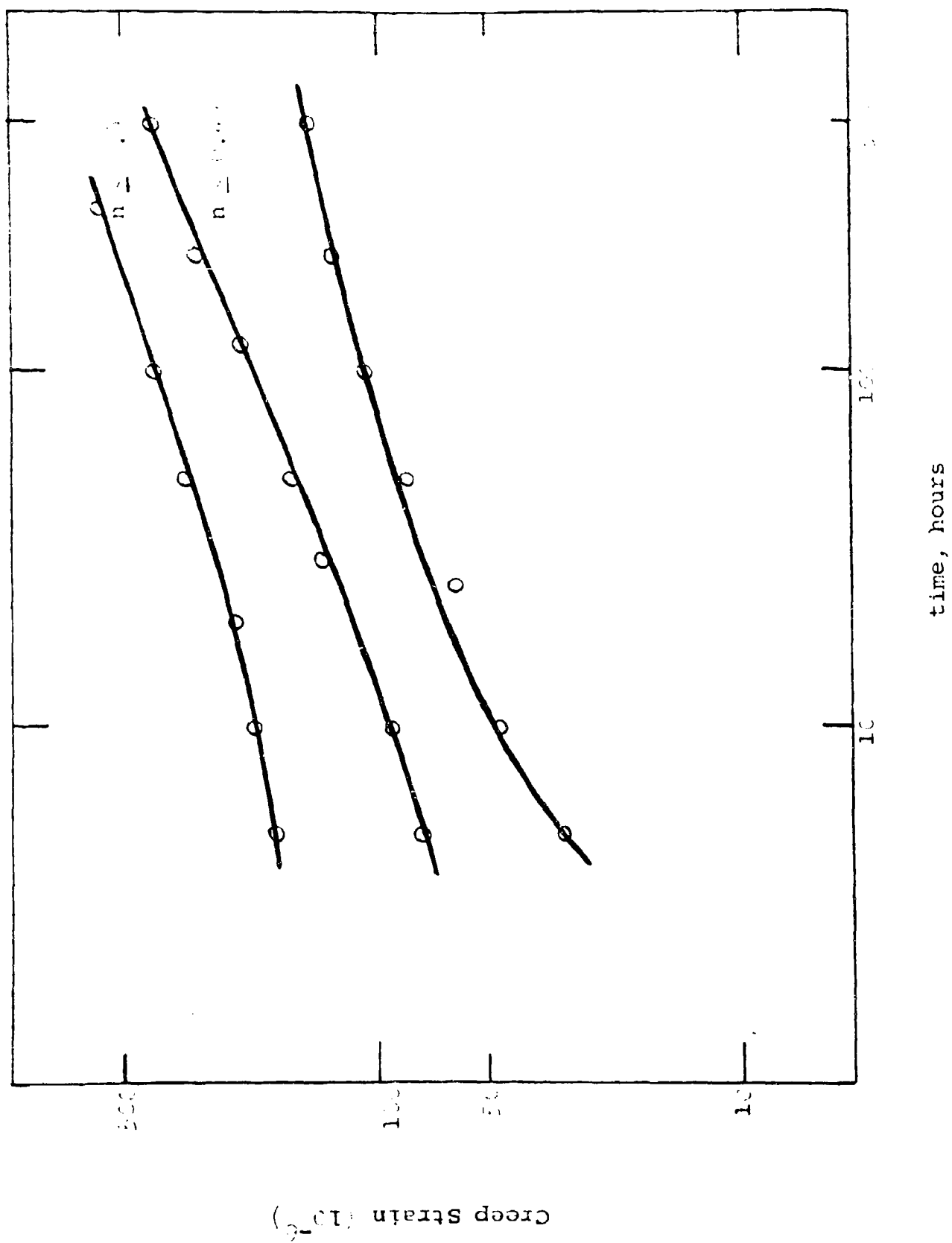


Figure 25 - Creep curves of 316 stainless steel at 200°F.

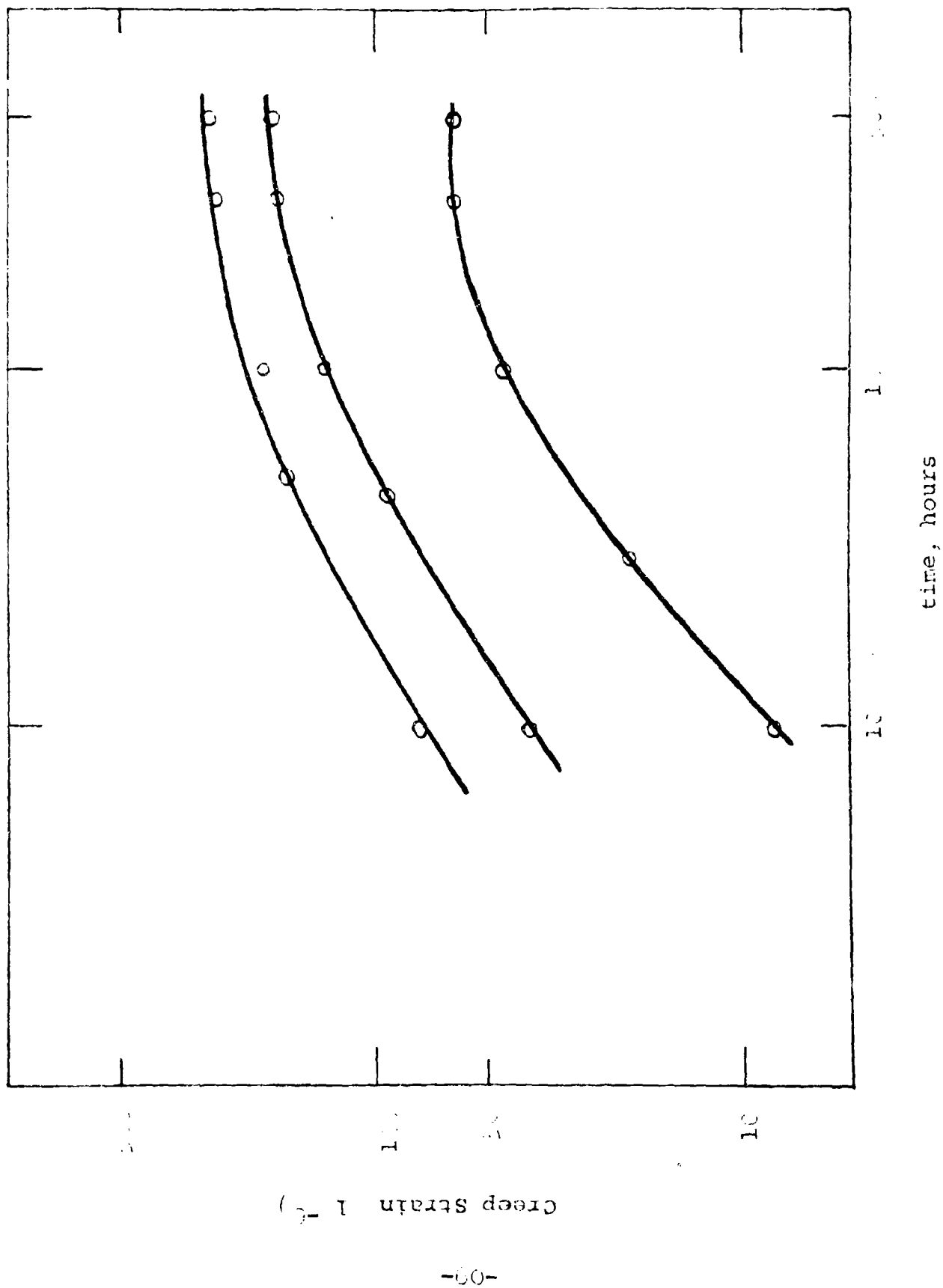


Figure 20 - Creep curves of 1001 aluminum at 100°F.

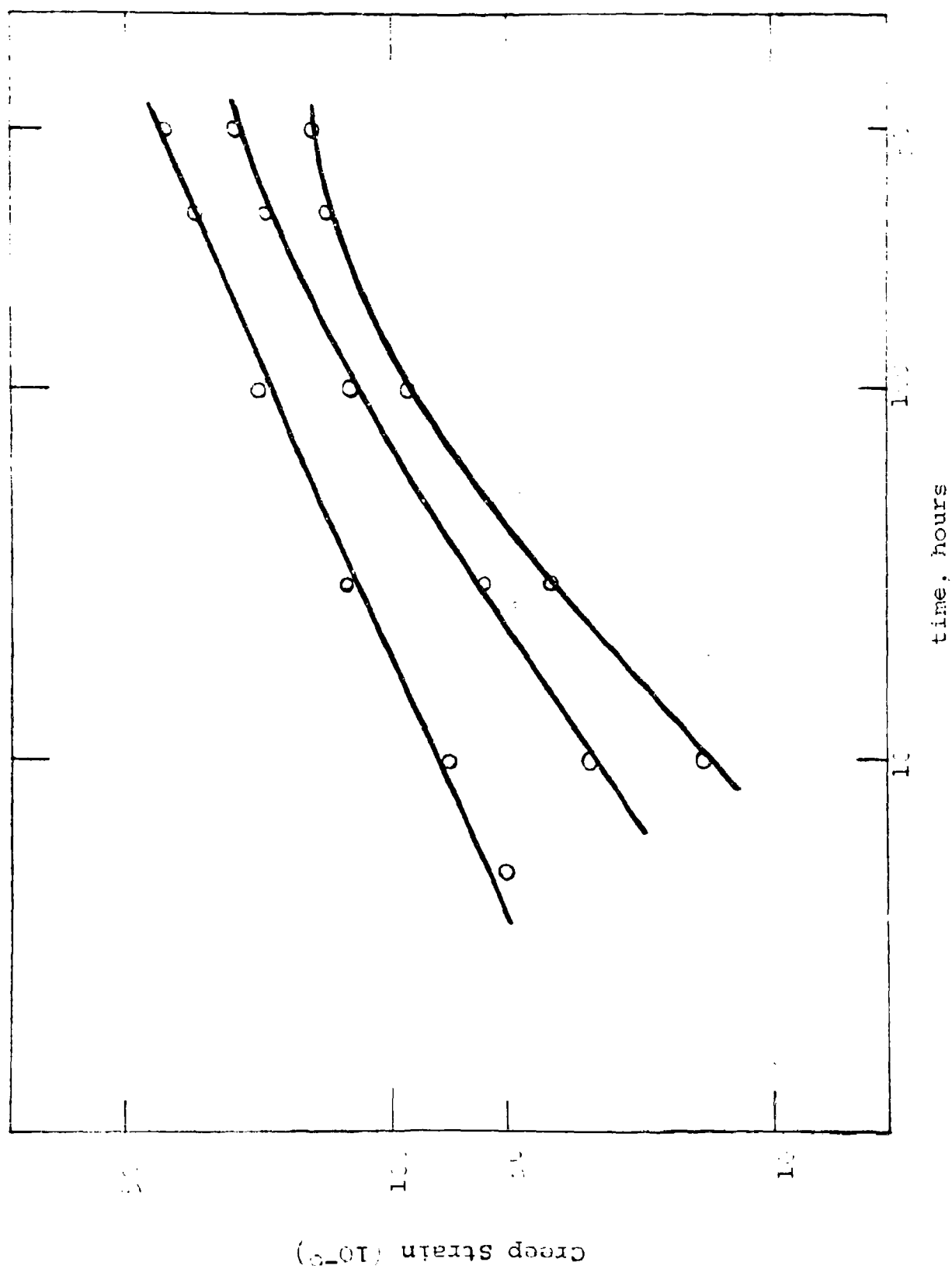


Figure 39 - Creep curves of 6061 aluminum at 180°F.

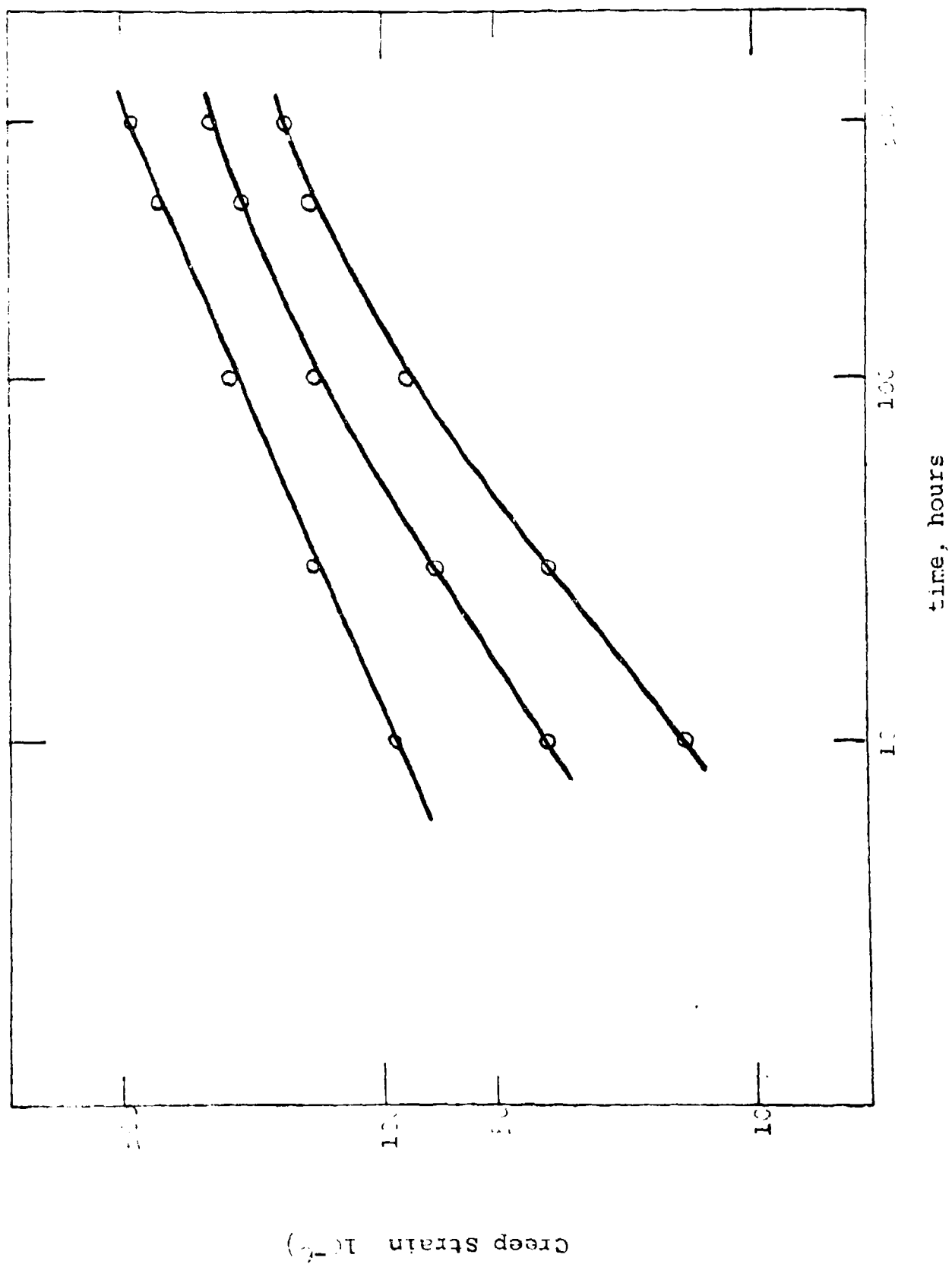


Figure 22 - Creep curves of 6061 aluminum at 250°F.



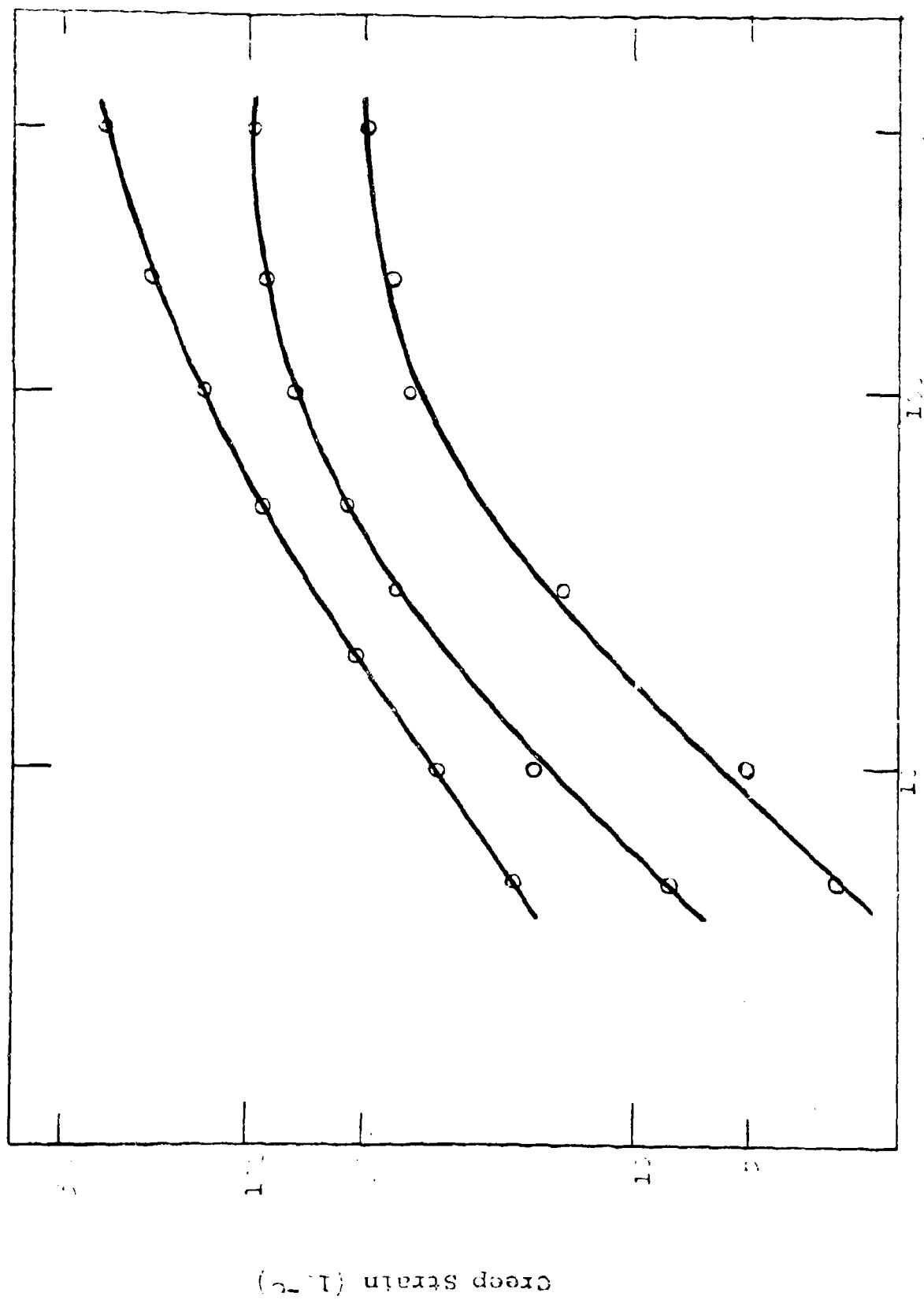


Figure 23 - Creep curves of AZ31A - Mg magnesium at 110°F.

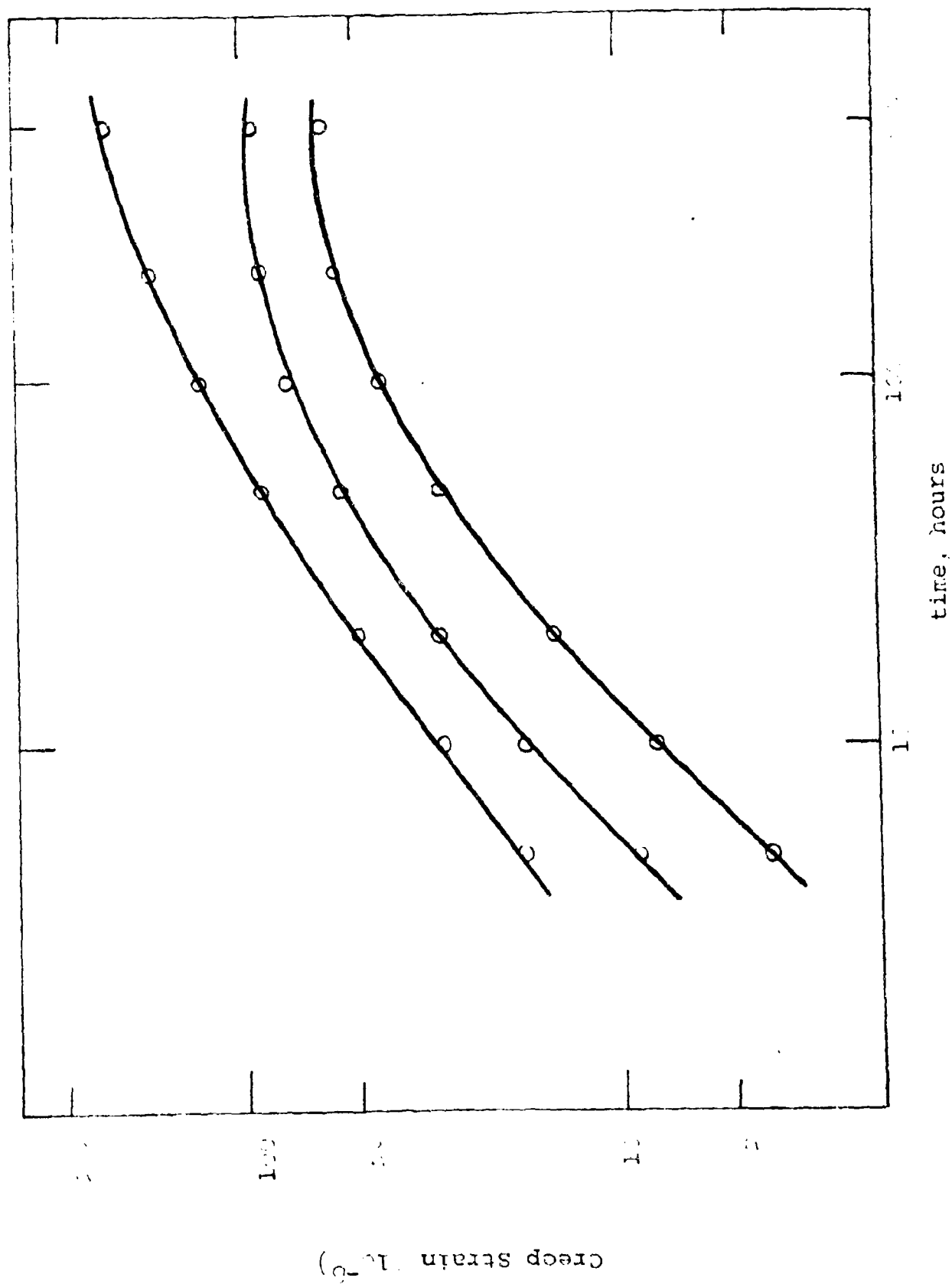


Figure 40 - Creep Curves of AZ31A - T<sub>6</sub> magnesium at 150°F.

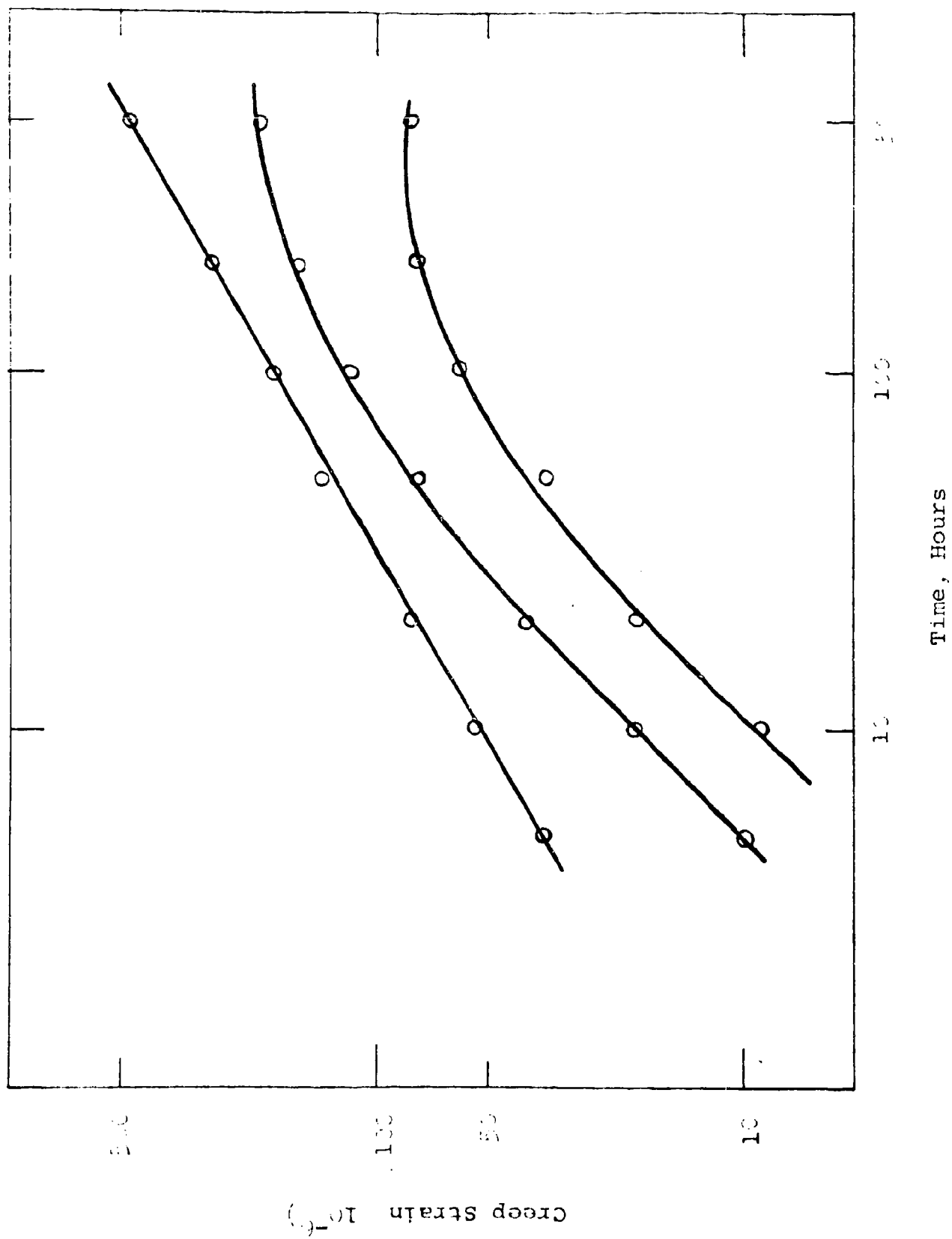


Figure 41 - Creep curves of AZ32A-Ti magnesium at 200°F.

**TABLE V****Creep Constants for Equation 14**

	<u>Invar</u> <u>36</u>	<u>310</u> <u>Stainless</u>	<u>356-T6</u> <u>Aluminum</u>	<u>6061</u> <u>Aluminum</u>	<u>AZ92A</u> <u>Magnesium</u>
n	0.3	0.33	0.45	0.5	-
k cm <sup>3</sup> /mole	0.3	0.2	1.5	0.2	-
A hr <sup>-1</sup>	1.6x10 <sup>-3</sup>	5.1x10 <sup>-4</sup>	2.5x10 <sup>-6</sup>	3.0x10 <sup>-7</sup>	-
Q cal/mole	48,000	62,000	21,000	24,000	-

Analysis of the activation energy,  $Q$ , yields results very close to reported values for the activation energy for self diffusion. Diffusional type creep, however, was not observed for the AZ92A magnesium except at the higher temperatures. This may be due to the low testing stresses at which diffusional creep may not predominate.

At stresses below the elastic limit small stress fluctuations will not result in instantaneous creep deformation since the stress-plastic strain curves have infinite slopes in this region. However, many dislocation sources are active at stresses below the elastic limit and these will operate, contributing to the creep strain until exhausted. As these sources are exhausted the creep rate should diminish eventually going to zero when no more active sources exist.

Following general reaction rate theory and assuming the rate of dislocation generation is of first order, the rate of exhaustion of active sources would be proportional to the concentration of active sources

$$-\frac{dN}{dt} = \rho N \quad (15)$$

which upon integration yields

$$N = N_0 e^{-\beta t} \quad (16)$$

Since the creep rate is given by

$$\frac{d\epsilon}{dt} = Nbp \quad (17)$$

where  $b$  is the Burgers vector,  $p$  the rate at which the dislocation sources operate and  $N$  the number of active sources, the creep strain is given by:

$$\epsilon = \frac{N_0 b p}{\beta} (1 - e^{-\beta t}) \quad (18)$$

where  $\frac{N_0 b p}{\beta}$  is the limiting strain after infinite time.

It is expected that the limiting strain should be directly proportional to the stress and the temperature, that is with increased temperature and at higher stresses the limiting strain increases. Analysis of the curves of Figures 27-41 at stresses below the elastic limit indicates that the limiting strain can be expressed as

$$\epsilon_{\infty} = \frac{N_0 b p}{\beta} = K \sigma_a^m T \quad (19)$$

where  $\sigma_a$  is the applied stress and  $T$  the absolute temperature.

Combining equations 18 and 19 gives a final expression for creep below the  $10^{-6}$  elastic limit of

$$\epsilon = A (1 - e^{-Bt}) \sigma_0^m T \quad (20)$$

The constants calculated from Figures 27-41 are tabulated in Table VI.

In summary, the results show that microcreep can be expressed by two relationships depending on whether the applied stress is larger or smaller than the  $10^{-6}$  elastic limit stress,  $\sigma_0$ .

Further analysis will aim at resolving the anomalous behavior of AZ92A magnesium. Efforts will be made to evaluate the constants from a theoretical model. The functional dependence of the creep strain on temperature and applied stress will be analyzed from theoretical considerations.

#### 4.3 Dimensional Changes Under Storage Conditions

The results of the evaluations of length changes in the five alloys under storage conditions at 75, 150 and 200°F are shown in Figures 42-46. Negative length changes were observed in all the alloys after 50 hours with the exception of the 6061 aluminum.

# TABLE VI

## Creep Constants for Equation

	Invar 36	310 Stainless Steel	356-T6 Aluminum	6061 Aluminum	AZ92P Magnesium
$\beta, \text{hr}^{-1}$	0.02	0.01	0.02	0.01	0.01
$n$	2.4	0.6	2.9	2.3	2.0
$A, (\text{psi-cal/mole})^{-1}$	$3 \times 10^{-12}$	$3.2 \times 10^{-3}$	$6.3 \times 10^{-15}$	$1.6 \times 10^{-10}$	$6.6 \times 10^{-9}$



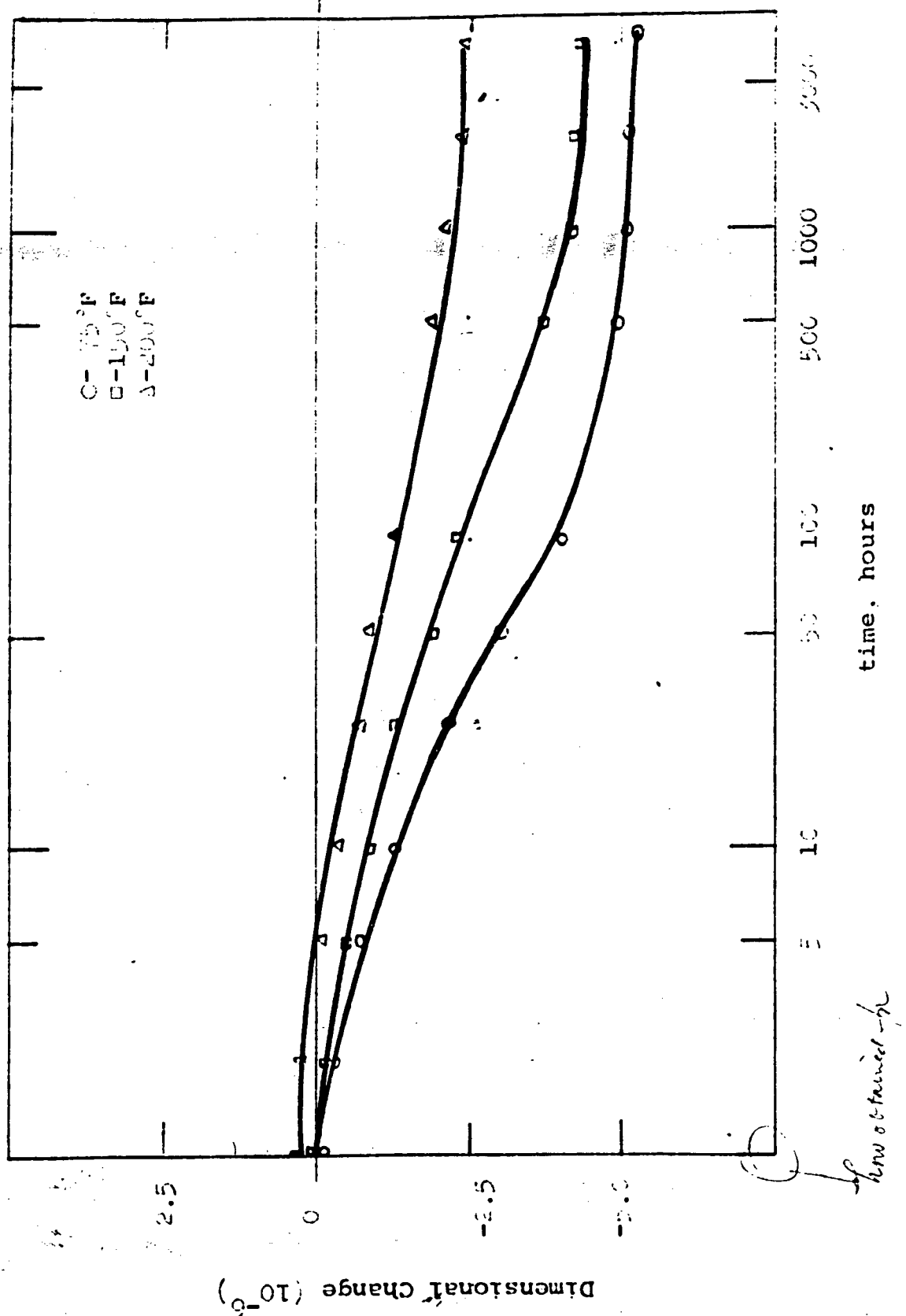


Figure 42 - Dimensional Change of free cut Invar 36 stored at 75, 150 and 200°F.

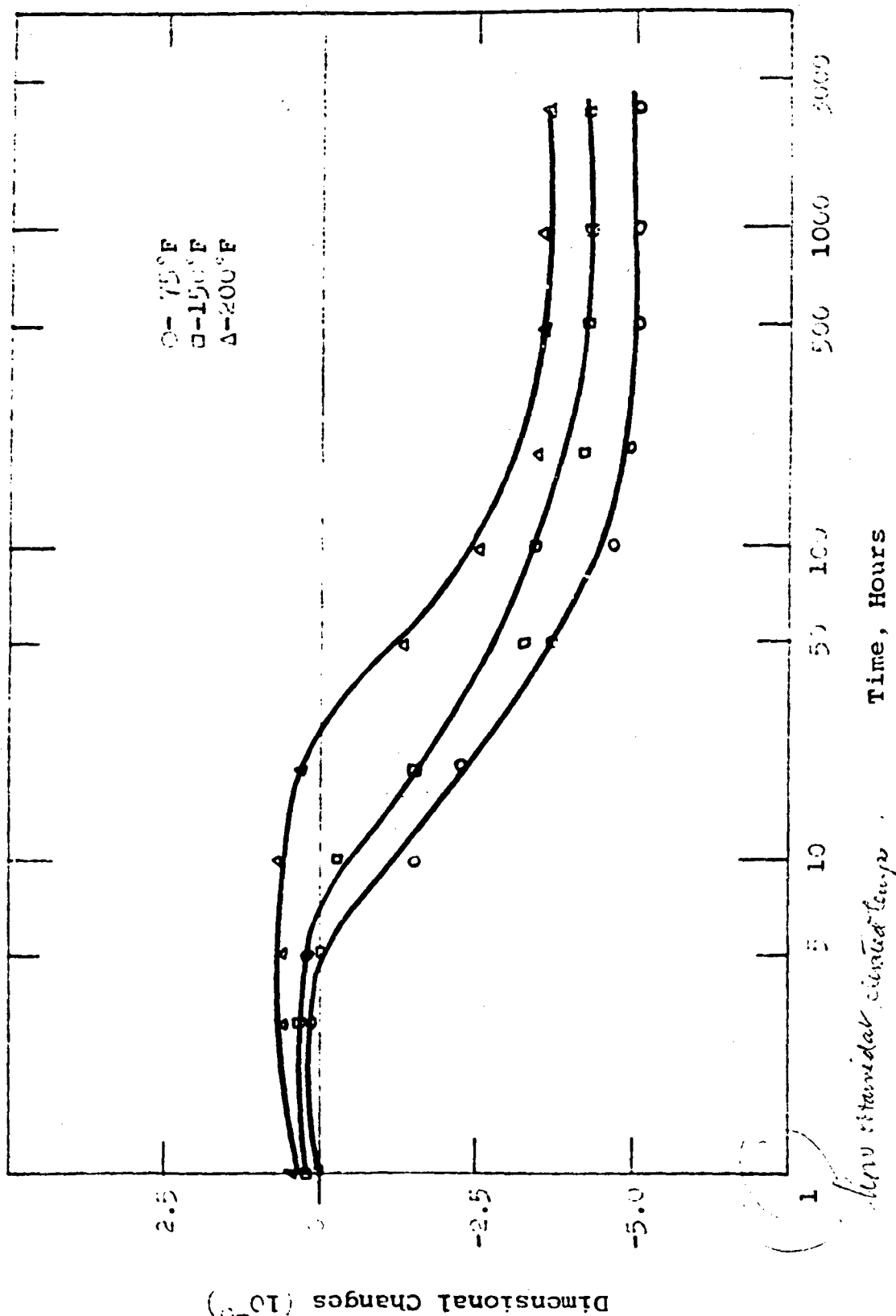


Figure 45 - Dimensional changes of 356-T6 Aluminum stored at 75, 150 and 200°F.

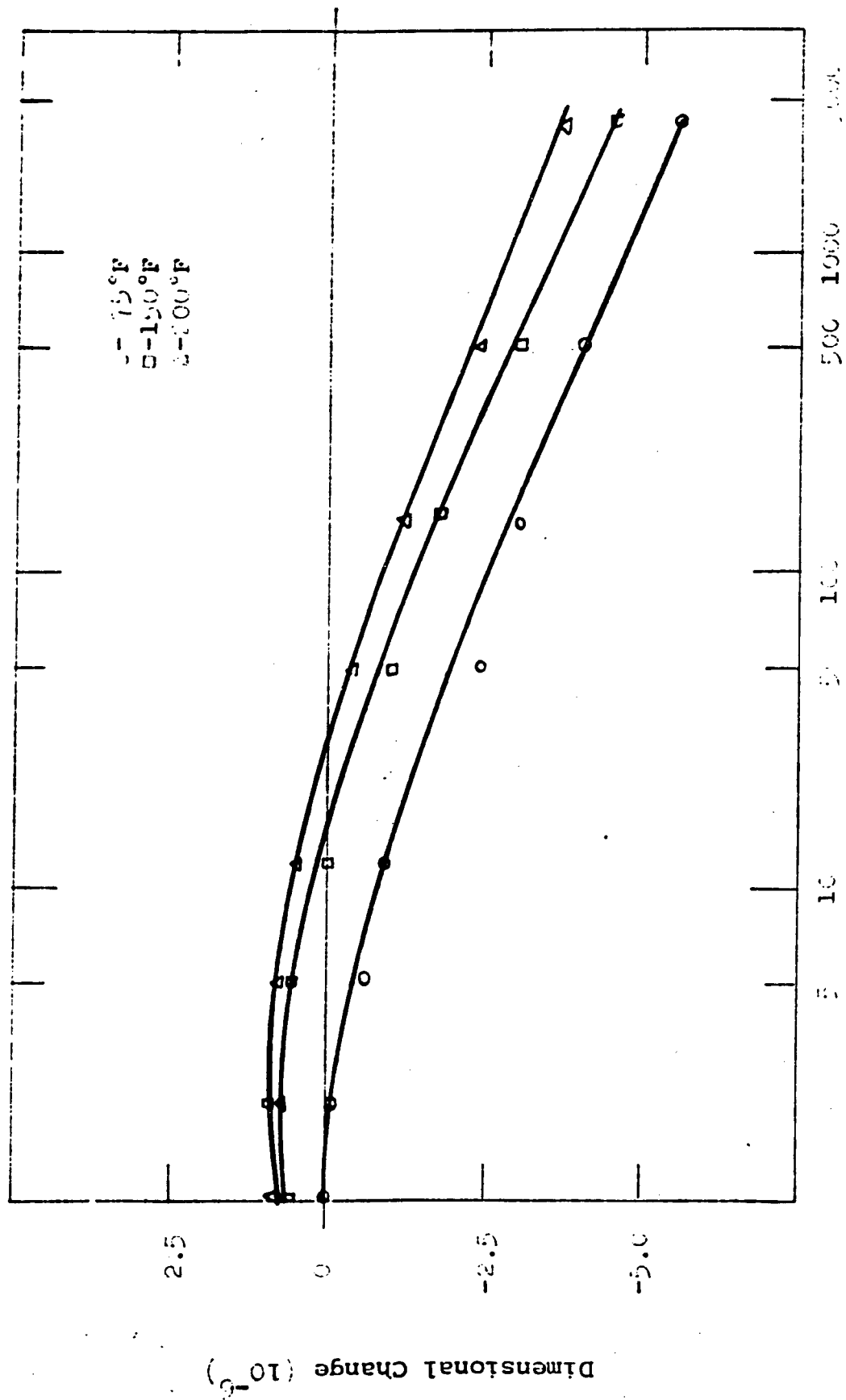


Figure 22 - Dimensional Changes of 316 stainless steel stored at 75, 150 and 200°F.

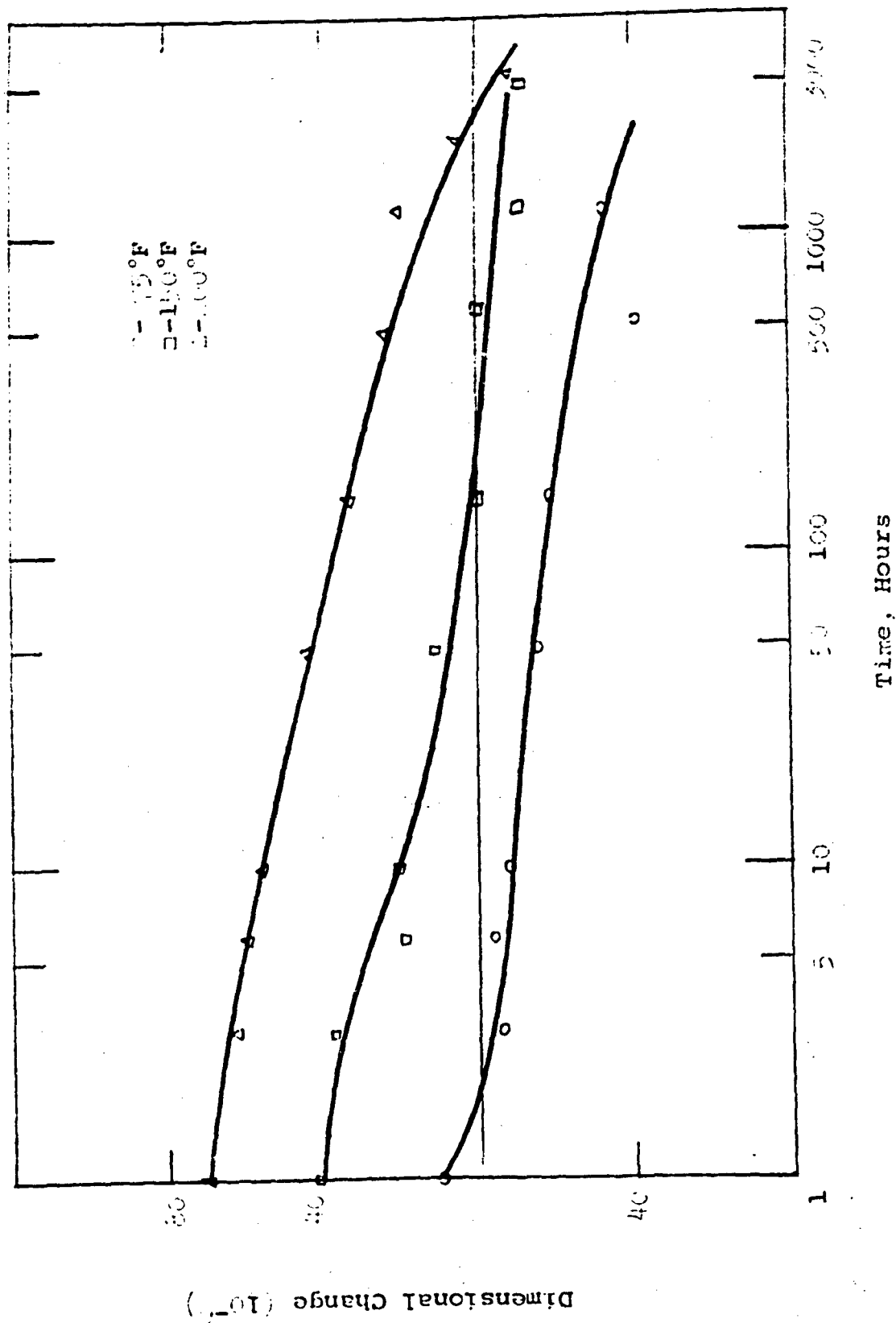


Figure 45 - Dimensional changes of 5051 Aluminum stored at 75, 150 and 200°F.

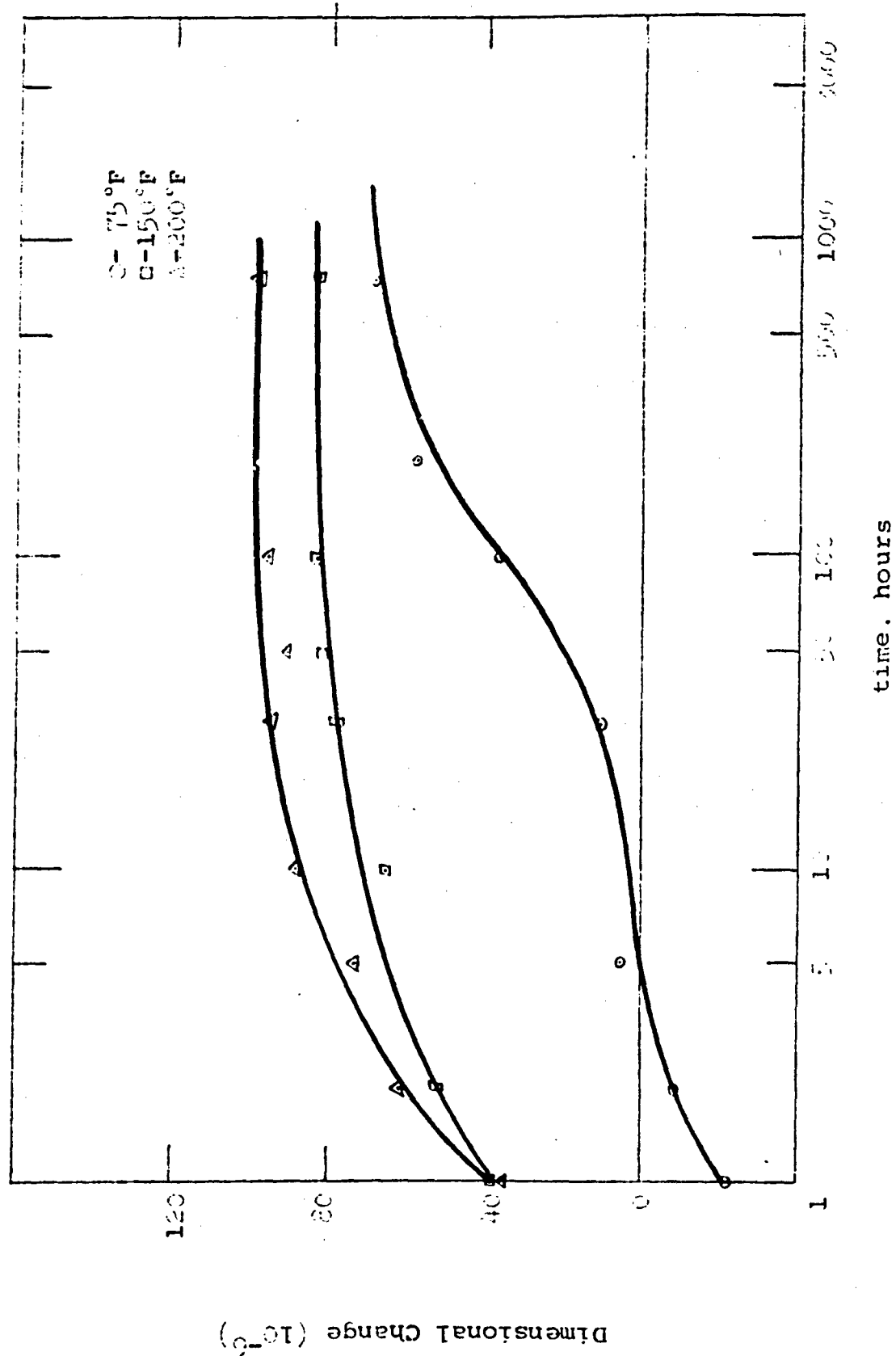


Figure 4C - Dimensional change of AZ1A magnesium stored at 75, 150 and 200°F.

The 356-T6 aluminum and 310 stainless steel showed a slight increase in length followed by a decrease in length. The 6061 Aluminum showed an initial negative change which slowly increased to an overall positive length change. The 356-T6 Aluminum showed the greatest dimensional instability. In all cases the magnitude of the dimensional changes were insignificant in comparison to the creep changes under load.

The measurements, although not complete, show dimensional changes similar to that reported by Lement and Averbach. (10)

## **5. DISTORTION MEASUREMENT FACILITY**

A facility for the determination of distortion in castings and welded structures after heat treating and machining operations was designed and the necessary equipment was purchased and constructed. The facility consists of the following items.

1. Hilger-Watts TA-1 autocollimator
2. Hilger-Watts 90° prism
3. 2 optically flat silvered mirrors
4. flat pyrex plate 12 x 12 x 1/2 inch
5. 2 standard blocks
6. precision 440C stainless steel balls 0.375 inch in diameter in several size ranges.

The complete assembly is mounted on a granite surface plate which is isolated from the floor by shock absorbers to minimize building vibration and ambiguity in the measurements.

The distortion specimen was rough machined to the dimensions of figure 47 on a milling machine. On the external faces 90° holes were rough drilled with a tap drill at the indicated points.

Following ageing a slot was cut as shown in Figure 47 with an Elox electrical discharge machining unit with a brass electrode. The surfaces were then milled with all faces parallel to within 0.001 inches. The conical holes were then finish machined in a Moore No. 3 jig-borer to a depth of 0.233 inch using an electronic depth stop. Carbide tooling was used to minimize tool wear. The hole dimension allows a 0.375 inch steel ball to rest at a depth of 0.100 inch in the distortion specimen.

The testing configuration is shown in Figure 48. The specimen rests on balls on the pyrex plate. The standard block is placed against the distortion block. For measurements in the horizontal position the standard block is fitted with a single steel ball. The mirror rests on two balls on the specimen and one on the standard. In this configuration a measurement in the change of height can be made, and by turning the autocollimator cross-hairs 90° the change in pitch of the specimen surface can be measured.



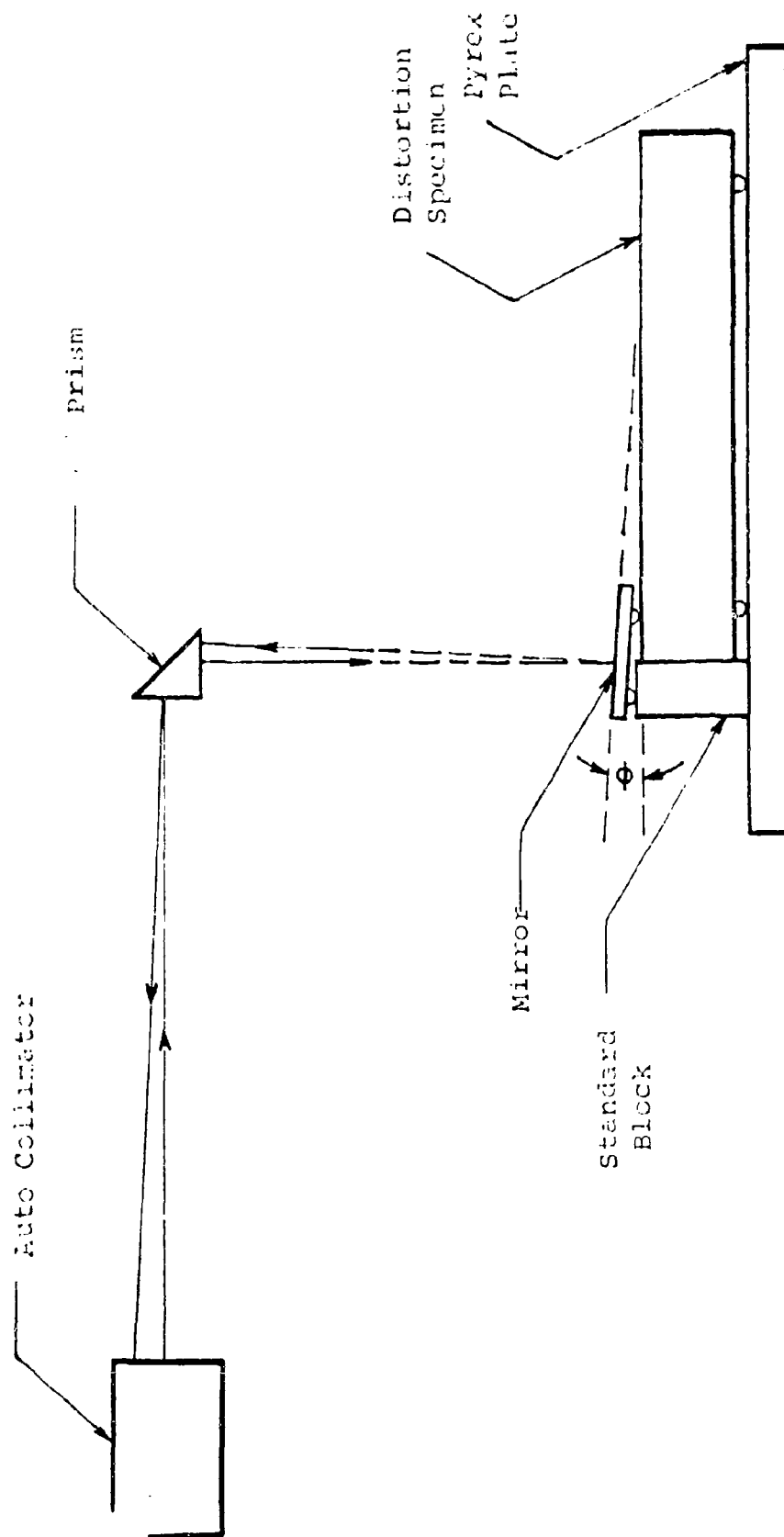


Figure 40 - Schematic View of Distortion Measuring Facility.

In the vertical position the standard block is fitted with two balls. The mirror rests on these two balls and one in the specimen. Measurements of the distortion across the slot are made by resting the mirror on three balls placed in holes on both sides of the slot. A beam of light from the autocollimator passes through the prism and is reflected by the mirror back through the prism and into the autocollimator. The angular divergence of the light beam in its passage appears as a shadow displaced from the cross-hairs of the instrument. This displacement can be read and from simple geometry converted to the angle  $\theta$  that the mirror makes with the distortion block. By measuring this angle  $\theta$  before and after a machining and/or heat treating operation, it is possible to measure the distortion due to these operations. By rearranging the specimen, linear distortion of the specimen can be measured in all directions.

In the event that distortion causes certain of the measurements to fall outside the field of the autocollimator, balls of different sizes can be calibrated and used.

Preliminary measurements of distortion in 356-T6 aluminum have been made which have demonstrated the technique's high resolution and usefulness. Distortion will be determined as a function of machining operations, age hardening and stress relief heat treatments for each of the five alloys evaluated in this program and for the three alloys to be evaluated in the coming year.

## 6. FUTURE WORK

This work will continue in the next year under a renewal contract. Dimensional stability evaluations will be conducted for HK31A-T6 magnesium-thorium, beryllium-copper and H-11 ausforming tool steel.

The analysis of microyield and microcreep data will continue in order to understand the mechanisms for these phenomena.

The measurements of dimensional changes under storage conditions will be carried out using autocollimation techniques. This technique will eliminate errors due to slight temperature variations and wear on the ends of the specimens from the comparator probe.

A testing program to evaluate distortion as a function of heat treating and machining operations will be initiated as outlined in section 5. The five alloys of the previous program as well as those mentioned above will be tested after fabrication procedures similar to those commonly used in structural applications of each alloy.

7. **REFERENCES**

1. Schetky, L.McD., M.I.T. Instrumentation Lab. Report R-137, January 1957.
2. Muir, H., Averbach, B.L. and Cohen, M., Trans. ASM, 47, 380 (1955).
3. Rosenfield, A.R. and Averbach, B.L., Acta. Met., 8 (1960) p. 624.
4. Wehrauch, P.F. and Averbach, B.L., M.I.T. Masters Thesis, January (1964).
5. Brown, W. and Lukens, K.F. Jr., Acta. Met., 9 (1961) p. 106.
6. Thomas, D.A. and Averbach, B.L., Acta. Met., 7 (1959) p. 69.
7. Feltham, P., Proc. Phys. Soc., B69 (1956) p. 1173.
8. Feltham, P. and Meakin, J.D., Acta. Met., 7 (1959) p. 614.
9. Suits, J.C. and Chalmers, B., Acta. Met., 9 (1961) p. 106.
10. Lument, B.E. and Averbach, B.L., M.I.T. Instrumentation Lab., Report R-95, December 1955.